Geophysical Journal International

Geophys. J. Int. (2023) **235,** 2870–2886 https://doi.org/10.1093/gji/ggad404
Advance Access publication 2023 October 16
GJI Seismology

Crustal deformation in the southeastern margin of the Tibetan Plateau: insights from broad-band Pg-wave attenuation tomography

Ruo-Jie Li,[1,2] Lian-Feng Zhao,[1,3] Xiao-Bi Xie[4] and Zhen-Xing Yao[1]

[1]*Key Laboratory of Earth and Planetary Physics, Institute of Geology and Geophysics, Chinese Academy of Sciences, Beijing* 100029*, China. E-mail: zhaolf@mail.igcas.ac.cn*
[2]*College of Earth and Planetary Sciences, University of Chinese Academy of Sciences, Beijing* 100049*, China*
[3]*Heilongjiang Mohe Observatory of Geophysics, Institute of Geology and Geophysics, Chinese Academy of Sciences, Beijing* 100029*, China*
[4]*Institute of Geophysics and Planetary Physics, University of California, Santa Cruz, CA* 95064*, USA*

Accepted 2023 October 14. Received 2023 October 11; in original form 2023 February 16

SUMMARY

The deformation mechanism in southeastern Tibet since the continental collision between the Indian and Eurasian plates could be explained by several models, including two major classic end-member models, the rigid-block extrusion model and the crustal flow model. Crustal channel flow is likely an important tectonic regime for properly explaining a large number of geological and geophysical observations but remains in competition with the block extrusion model. Consequently, detecting ductile flow connectivity would play a key role in understanding the tectonic evolution of the southeastern Tibetan Plateau. Here, we established a high-resolution broad-band Q_{Pg} model for the crust in SE Tibet by using a joint inversion tomography method based on both single- and two-station Pg data. We verified the stability of the Q_{Pg} tomography by comparing the Q_{Pg} values at 1 Hz between the joint inversion and the two-station method. Two low-Q_{Pg} zones were observed, isolated by the high-Q_{Pg} Emeishan large igneous province (ELIP). Strong Pg attenuation beneath the Songpan-Ganzi Block and Western Sichuan Block may indicate the presence of crustal material flow due to relatively weak rheological strength. Cooled basaltic magma remnants in the inner zone of the ELIP likely block the southeastward migration of crustal materials driven by the gravity and lateral pressure gradient, and restrict the flow to the Western Sichuan Block, resulting in surface uplift and crustal thickening. Strong Pg attenuation near the Xiaojiang Fault and the Red River Fault may result from mantle upwelling in this region. Our Q_{Pg} model, combined with previous results, suggests that the tectonic deformation in the southeastern Tibetan Plateau has been mainly controlled by the effects of crustal channel flow and asthenospheric upwelling since the Late Miocene.

Key words: Asia; Body waves; Seismic attenuation; Seismic tomography; Crustal structure; Large igneous provinces.

HIGHLIGHTS

(i) A high-resolution broad-band Pg-wave attenuation model is obtained for the crust in SE Tibet.

(ii) Two independent strong Pg attenuation zones in the crust are separated by the Emeishan large igneous province.

(iii) The crustal deformation in SE Tibet likely results from the crustal material flow and hot mantle upwelling.

1 INTRODUCTION

The southeastern margin of the Tibetan Plateau has accommodated the escape and extrusion of lithospheric materials since the collision between the Indian and Eurasian plates at ∼55 Ma (Molnar & Tapponnier 1975; Tapponnier *et al.* 2001). SE Tibet is the transition zone from a vast high-elevation plateau (>4000 m) to a relatively low-elevation foreland, accompanied by large-scale fault systems (Fig. 1). The lithospheric material rotates clockwise around the Eastern Himalaya Syntaxis (EHS) along these major faults, as revealed by GPS measurements (Holt *et al.* 1991; Zhang *et al.* 2004). However, the detailed mechanisms of surface uplift and crustal deformation in SE Tibet remain unclear, and the controversy focuses on how to balance two classical end-member models, the rigid-block extrusion (Molnar & Tapponnier 1975; Tapponnier *et al.* 1990) and the mid-lower crustal channel flow (Royden *et al.* 1997; Clark & Royden 2000). However, in recent years, these two competing models have been coordinated into a combined model, which emphasizes

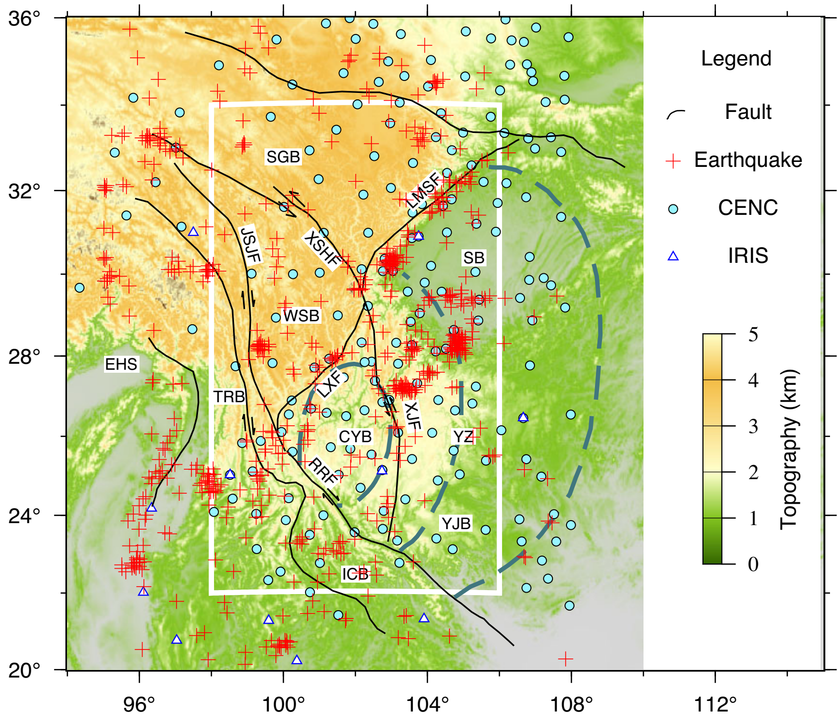

Figure 1. Topographic map showing the locations of major faults (black lines), seismic stations (circles and triangles) and regional earthquakes (red crosses) in SE Tibet. CYB: Central Yunnan Block; EHS: Eastern Himalaya Syntaxis; ICB: Indo-China Block; SB: Sichuan Basin; SGB: Songpan-Ganzi Block; TRB: Three-River Orogenic Belt; WSB: Western Sichuan Block; YJB: Youjiang Basin; YZ: Yangtze Block. JSJF: Jinshajiang Fault; LMSF: Longmenshan Fault; LXF: Lijiang-Xiaojinhe Fault; RRF: Red River Fault; XJF: Xiaojiang Fault; XSHF: Xianshuihe Fault. CENC: China Earthquake Networks Center; IRIS: Incorporated Research Institutions for Seismology. Dark green dashed lines divide the Emeishan large igneous province (ELIP) into the inner, intermediate, and outer zones from west to east. Note that the CYB and the inner zone of the ELIP are nearly geographically coincident.

the joint control of these two mechanisms in SE Tibet (Liu *et al.* 2014; Bao *et al.* 2015; Qiao *et al.* 2018; He *et al.* 2021). The key to resolving the debate lies in whether crustal flow exists and, if it exists, what role it played in the tectonic evolution of SE Tibet.

Many observations support a mechanically weak middle-to-lower crust, which provides a fundamental basis for the existence of crustal flow beneath SE Tibet. These observations include the widely distributed low-velocity zones in the mid-lower crust (Liu *et al.* 2014), high electrical conductivity (Bai *et al.* 2010), strong Lg-wave attenuation (Zhao *et al.* 2013; He *et al.* 2021) and high heat flow (Hu *et al.* 2000; Jiang *et al.* 2019) in this region. With the blockage imposed by the high-velocity and high-density Emeishan large igneous province (ELIP) in this region, the extent of possible crustal flow remains controversial. Some studies suggested that the low-viscosity crustal flow is likely stopped in SE Tibet (Liu *et al.* 2014), while others concluded the flow is divided into two branches that bypass the ELIP and extend farther southeastward (Qiao *et al.* 2018; Dai *et al.* 2020). Two geophysical anomalies are commonly observed on both sides of the ELIP. Ambient noise tomography revealed two isolated low-velocity zones separated by the high-velocity region in the inner zone of the ELIP (Yao *et al.* 2008; Chen *et al.* 2014). Magnetotelluric profiles also depicted two main conductors located on both sides of the core of the ELIP (Li *et al.* 2020). However, the lack of strong radial anisotropy in the mid-lower crust questions the existence of large-scale directional crustal flow (Bao *et al.* 2020). Thermomechanical modelling results suggested that partial melting in the crust is a self-consistent product of crustal thickening, challenging the previous view that crustal thickening is caused by crustal inflow (Chen & Gerya 2016). Therefore, whether the two geophysical anomalies separated by the ELIP are homologous and both the result of crustal flow still require more evidence and insights from high-precision crustal models.

Seismic wave attenuation, commonly quantified by the quality factor Q, is sensitive to the properties and status of crustal materials, for example mineral composition, cracks and faults of multiple scales, fluid content, temperature and partial melting, (Winkler & Nur 1982; Karato & Spetzler 1990; Kong *et al.* 2013; Amalokwu *et al.* 2014). They either directly affect the anelastic properties of the material causing the intrinsic attenuation, or generate heterogeneities of different scales contributing to the scattering attenuation. Therefore, the quality factor Q can be a useful indicator of the rheology property of the material, and potentially related to the crustal material escape. He *et al.* (2021) developed a broadband Lg-wave attenuation model for the crust of the southeastern Tibetan Plateau, revealing a complicated connectivity of crustal material flow. In this study, we aim to establish a Pg wave Q model for the crust in SE Tibet to explore the connectivity and origins of crustal attenuations through comparison with Lg-wave Q anomalies and provide additional constraints on the deformation mechanism of the crust in this region.

Pg is the first arrival phase at local distances, and the second after Pn beyond the crossover distance in regional seismograms (Pyle *et al.* 2017), with epicentral distances ranging from 1° to 10° (Nicolas *et al.* 1982). According to the definition of the International Association of Seismology and Physics of the Earth's Interior (IASPEI), at short distances, the Pg phase is the upgoing

P wave from an upper crustal source or the *P* wave bottoming in the upper crust; at a greater distance, it is composed of multiple *P*-wave reverberations inside the whole crust with a group velocity of approximately 5.8 km s^{-1} (Storchak *et al.* 2003). In this study, we consider the Pg phase in a broad definition that contains not only the early parts of the most direct arrivals but also the later parts composed of the whole-crust reverberations (Sato & Fehler 2012). The Pg phase with an epicentral range from 70 to 800 km and within a group velocity window between 6.3 and 5.4 km s^{-1} was adopted in this study (Yang *et al.* 2021a). In this case, Pg attenuation can reflect the whole crust structure.

Pg-wave attenuation tomography has been developed and applied over the past decades. The two-station method (Bao *et al.* 2011a; Singh *et al.* 2019), the reverse two-station/event method (Bao *et al.* 2011b), and the simultaneous multiphase approach (Pasyanos *et al.* 2009a) are generally used for Pg-wave attenuation measurements. Both the two-station and the reverse two-station/event methods reduce the trade-off between the source and attenuation terms by eliminating the source term from the data, but their resolutions are relatively lower due to limited data. The simultaneous multiphase approach provides better path coverage and higher resolution than the two-station measurements (Pasyanos *et al.* 2009b), but there are certain trade-offs among different phases and between the source and attenuation terms. In this study, we developed a Pg-wave attenuation tomography method based on a joint inversion of single- and two-station data, generalized from Lg-wave *Q* tomography (Zhao *et al.* 2010, 2013; Zhao & Xie 2016). This method not only has the advantage of the two-station method that reduces the trade-off between the source and attenuation term but also greatly improves the tomographic resolution by adding single-station data. With the proposed method, we obtained a high-resolution broad-band Pg-wave attenuation model of the crust in SE Tibet and surrounding regions using high-density seismic array data in this region. In terms of the potential crustal material escape indicated by low-Q_{Pg} anomalies, we determined the spatial distribution and connectivity of crustal flow channels and further explored their implications for tectonic evolution in SE Tibet.

2 DATA

We collected 60 025 vertical-component seismograms from 649 seismic events recorded by 201 stations between January 2010 and May 2021 in SE Tibet (Fig. 1). The seismic stations include 190 stations from the China Earthquake Networks Center (CENC) and 11 stations from the Incorporated Research Institutions for Seismology (IRIS) Data Management Center. The high-density distribution of seismic stations guarantees dense ray coverage and high tomographic resolution. Seismic events within the upper crust with magnitudes between m_{b} 4.0 and 6.5 and distances between 70 and 800 km were selected (Fig. S1). The Pg waves contain both direct rays and multiply reflected rays (Krishna & Ramesh 2000; Sato & Fehler 2012) and hence can be used to investigate the attenuation characteristics of the whole crust. Even though a small amount of energy leaks into the upper mantle to form Pn waves (Shaw & Orcutt 1984), we neglect these energies and consider them as Pg geometric spreading.

Based on a group velocity window between 6.3 and 5.4 km s^{-1} (Yang *et al.* 2021a), we sampled Pg waves, and an equal-length time window is used to sample the pre-P noise series. Their spectral amplitudes were calculated using the Fourier transform. We selected 66 discrete frequencies log-evenly between 0.05 and 20 Hz with an interval of 0.04 log unit. The spectral amplitudes of Pg waves and pre-event noise were sampled at individual frequencies, and the signal-to-noise ratios (SNRs) were calculated. Data with SNR <2.0 were dropped (e.g. Bao *et al.* 2011a; Zhao *et al.* 2013; Yang *et al.* 2021a). Thus, we constructed a dataset of Pg spectra. The denoising process was conducted according to Zhao *et al.* (2010)

$$A_{\mathrm{sig}}^2(f) = A_{\mathrm{obs}}^2(f) - A_{\mathrm{noi}}^2(f), \tag{1}$$

where f represents the reference frequency. A_{sig}, A_{obs} and A_{noi} are for true, observed and noise spectral amplitudes at frequency f, respectively. As an example, Fig. 2 illustrates this process, where the seismogram was generated by an earthquake on 5 February 2021, and recorded by station YN.BAS at a distance of 479.8 km (Fig. 2a). After removing the instrument response, we obtained the ground velocity (Fig. 2b) and its envelope (Fig. 2c), where the pre-*P* noise and Pg windows are highlighted in Figs 2(d) and (e). The sampled Pg waveform and pre-*P* noise are shown in Figs 2(d) and (e). Fig. 2(f) illustrates the Pg wave and pre-P noise spectra, and Fig. 2(g) shows the corresponding signal-to-noise ratios. The final denoised Pg-wave spectrum at discrete frequencies with a signal-to-noise ratio ≥2.0 is shown in Fig. 2(h). Finally, we constructed a dataset with Pg-wave amplitudes at 66 reference frequencies as the basis for the subsequent Q_{Pg} inversion.

3 METHODS

3.1 Modelling of pg amplitude

The Pg-wave spectral amplitude can be expressed as (Xie & Mitchell 1990; Bao *et al.* 2011a)

$$A(f, \Delta) = S(f) \cdot G(\Delta) \cdot \Gamma(f, \Delta) \cdot P(f) \cdot r(f), \tag{2}$$

where f is the frequency, Δ is the epicentral distance, $A(f, \Delta)$ is the Pg-wave displacement spectrum and $S(f)$ is the source spectrum. By adopting the Brune (1970) source model, it can be expressed as

$$S(f) = \frac{M_0 R^P}{4\pi\rho v_p^3} \cdot \left[1 + \frac{f^2}{f_c^2}\right]^{-1}, \tag{3}$$

where M_0 is the seismic moment, R^P is the average radiation pattern, taking to be 0.44 (from Boore & Boatwright 1984) ρ and v_p are the density and *P*-wave velocity in the source region and are set to be 2.7 g cm^{-3} and 5.8 km s^{-1}, respectively (Liu *et al.* 2021), and f_c is the corner frequency. $G(\Delta)$ is the geometric spreading of the Pg wave and can be expressed as

$$G(\Delta) = (1/\Delta_0)(\Delta_0/\Delta)^m, \tag{4}$$

where Δ_0 is a reference distance, which is 70 km here (e.g. Pyle *et al.* 2017), and m= 0.5 is the geometric spreading factor (Street *et al.* 1975), which has been widely applied in previous studies of Pg-wave attenuation (e.g. Walter *et al.* 2007; Pasyanos *et al.* 2009a; Pyle *et al.* 2017; Singh *et al.* 2019). In contrast, some authors used different parameters for the Pg geometric spreading. For example, Paul *et al.* (1996) used body waves and coda waves to estimate the seismic attenuation in the northern Tien Shan, with a geometric spreading of 1.5. Bao *et al.* (2011a) used a Pg geometric spreading factor of 1.3 in the northern Middle East. Using different geometric spreading may slightly change the general Pg *Q* levels in a broad area, but will not change detailed geographic Pg-*Q* distribution patterns. Therefore, we prefer to use the Pg geometric spreading factor of 0.5 in eq. (4), and it is consistent with multiply-reflected body waves trapped in the crust (Walter *et al.* 2007). $\Gamma(f, \Delta)$ is the

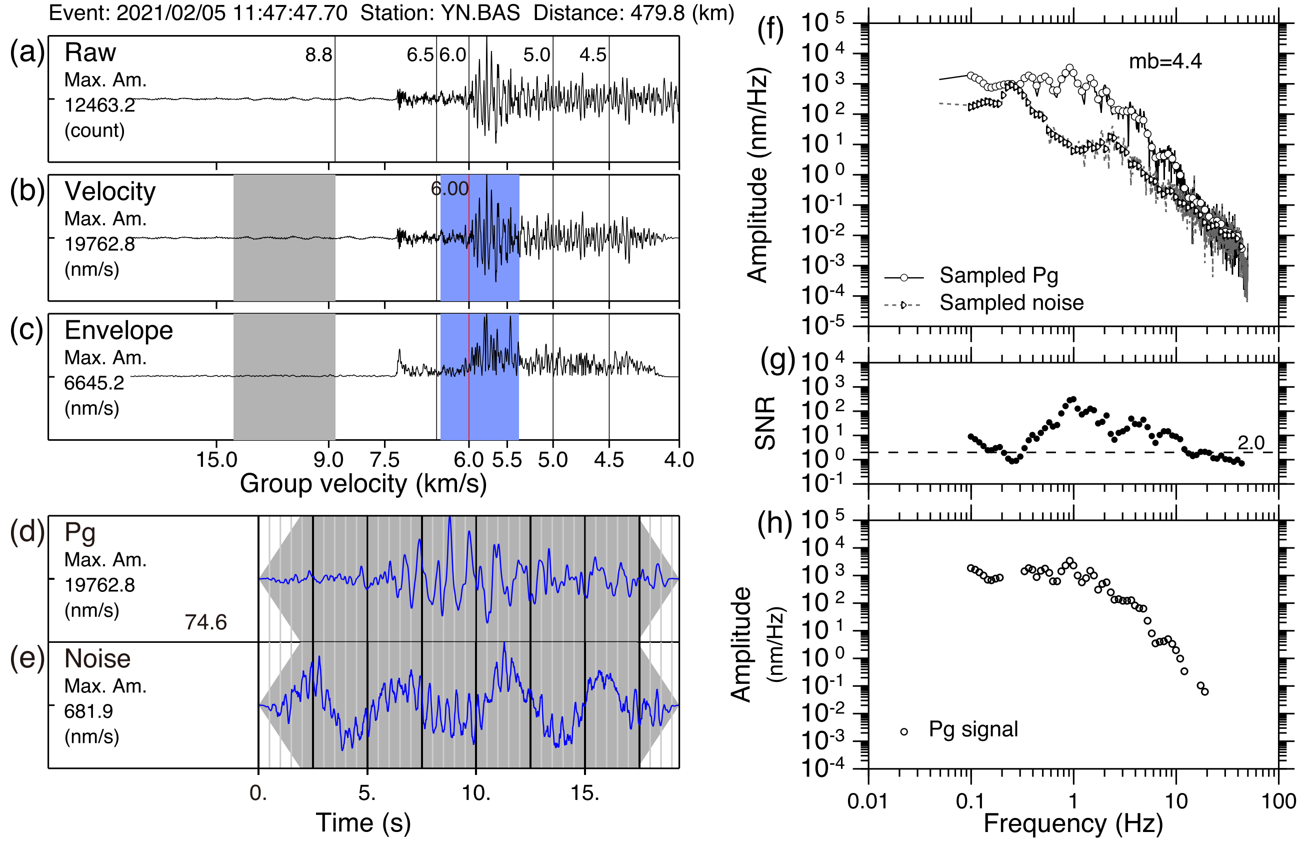

Figure 2. An example of the Pg-wave data pre-processing. (a) Original seismic record observed at station YN.BAS for an event on 5 February 2021, (b) velocity record after removing the instrument response and (c) the envelope of the waveform filtered between 0.5–5.0 Hz, used to quality control the Pg energy arriving within its sampling window, where the grey and blue areas are pre-P noise and Pg sampling windows, respectively. (d, e) Sampled Pg phase and pre-P noise. (f) Pg wave and pre-*P* noise spectra, (g) signal-to-noise ratio and (h) Pg-wave spectra at individual frequencies with SNR ≥2.0 and corrected for the noise using eq. (1).

attenuation term and can be expressed as

$$\Gamma(f,\Delta) = \exp\left[-\frac{\pi f}{V}\int_{ray}\frac{ds}{Q(x,y,f)}\right] = \exp\left\{-\frac{\pi f}{V}\left[\sum_{n=1}^{N}\int_{n}\frac{ds}{Q(x,y,f)}\right]\right\}, \tag{5}$$

where V is the Pg wave group velocity, which is set to be 6.0 km s^{-1} in this study, $\int_{ray} ds$ is the integral along the great circle ray path, and $Q(x, y, f)$ is the apparent Q value at a frequency f and geographic location (x, y). For attenuation tomography, we partitioned the Q model into rectangular grids and discretized the integral over the ray into a summation over multiple cells, where n represents the nth rectangle cell through which the ray passes, $\int_n ds$ represents the integration along the ray segment in the nth rectangle, and N is the total number of segments along the ray. $P(f)$ is the site response, and $r(f)$ is a random error. For simplicity, we neglected the random error term by assuming that $r(f) = 1$.

3.2 Joint attenuation inversion using single-station and two-station data

According to eq. (2), the observed single-station Pg spectral amplitude generated by event k and observed at station j can be expressed as (refer to Fig. 3a)

$$A_{kj}(f,\Delta) = S_k(f)\cdot G_{kj}(\Delta)\cdot \Gamma_{kj}(f,\Delta)\cdot P_j(f)\cdot r_{kj}(f). \tag{6}$$

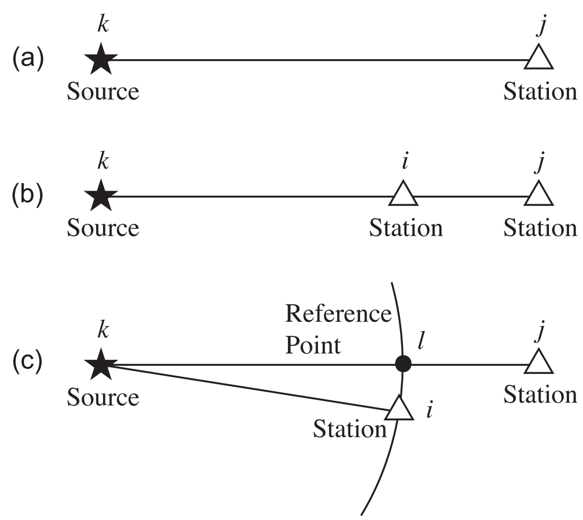

Figure 3. Schematic diagrams of the geometric distributions of seismic sources and stations, with (a) single-station data, (b) two-station data and (c) relaxed two-station requirement. To make the approximation valid, the distance between locations i and l should be smaller than half an inversion grid.

If event k is recorded by two stations i and j, and both stations are aligned along the same great circle ray path with the source (as shown in Fig. 3b), the Pg spectral amplitude ratio between these two stations can be expressed as

$$A_{ij}^{ratio} = \frac{A_{kj}}{A_{ki}} = \left(\frac{\Delta_{kj}}{\Delta_{ki}}\right)^{-1/2} \cdot \exp\left[-\frac{\pi f}{V}\int_i^j \frac{ds}{Q(x,y,f)}\right] \cdot \frac{P_j}{P_i}, \tag{7}$$

where the integral $\int_i^j ds$ are over their common ray path section from i to j, the random errors are neglected, that is $r_{ki}(f) = r_{kj}(f) = 1$. In most cases, the source and stations are not perfectly aligned along a great circle (refer to Fig. 3c). To increase the available two-station data, we can relax the above requirement by creating a reference point l on the line between k and j, and required that $\Delta_{ki} = \Delta_{kl}$ and the distance between i and l is less than half of the dimension of an inversion cell to validate the approximation. Under this approximation, the two-station Pg spectral amplitude ratio can be obtained as

$$A_{lj}^{ratio} \approx \frac{A_{kj}}{A_{ki}} = \left(\frac{\Delta_{kj}}{\Delta_{kl}}\right)^{-1/2} \cdot \exp\left[-\frac{\pi f}{V}\int_l^j \frac{ds}{Q(x,y,f)}\right] \cdot \frac{P_j}{P_i}. \tag{8}$$

For inversion, from the single station data, by taking the natural logarithm of eq. (6), we obtain

$$\ln\left[A_{kj}(f,\Delta)\right] = \ln\left[S_k(f)\right] + \ln\left[G_{kj}(\Delta)\right] - \frac{\pi f}{V}\cdot\int_k^j \frac{ds}{Q(x,y,f)} + \ln\left[P_j(f)\right]. \tag{9}$$

Assuming that the attenuation, source function and site response can all be separated into a background part and a perturbation, according to Zhao *et al.* (2010),

$$\frac{1}{Q(x,y,f)} \approx \frac{1}{Q^0(x,y,f)} - \frac{\delta Q(x,z)}{\left[Q^0(x,y,f)\right]^2}, \tag{10a}$$

$$\ln\left[S_k(f)\right] = \ln\left[S_k^0(f)\right] + \delta\ln\left[S_k(f)\right], \tag{10b}$$

and

$$\ln\left[P_j(f)\right] = \ln\left[P_j^0(f)\right] + \delta\ln\left[P_j(f)\right]. \tag{10c}$$

Consequently, we have

$$\begin{aligned}&\ln\left[A_{kj}(f,\Delta)\right] - \ln\left[S_k^0(f)\right] - \ln\left[G_{kj}(\Delta)\right] + \tfrac{\pi f}{V}\cdot\int_k^j \tfrac{ds}{Q^0(x,y,f)} - \ln\left[P_j^0(f)\right]\\ &= \tfrac{\pi f}{V}\cdot\int_k^j \tfrac{\delta Q(x,z)}{\left[Q^0(x,y,f)\right]^2} + \delta\ln\left[S_k(f)\right] + \delta\ln\left[P_j(f)\right]\end{aligned}, \tag{11}$$

where terms with a superscript 0 represent the initial value or the intermediate value during the inversion iteration. The right-hand side of this equation represents the difference in the spectral amplitude before and after an iteration, which contains the disturbances of the attenuation, source and site response and is represented by h_{kj},

$$h_{kj} = \frac{\pi f}{V}\cdot\left[\sum_{n=1}^{N}\int_n \frac{\delta Q(x,z)}{\left[Q^0(x,y,f)\right]^2}\right] + \delta\ln\left[S_k(f)\right] + \delta\ln\left[P_j(f)\right]. \tag{12}$$

Note, similar to that in eq. (5), we have discretized the integral over the ray path into a summation in the above equation. With eqs (11) and (12), the spectral amplitude residual can be mapped to the sources and site responses, as well as attenuation distributions at all individual model cells, forming a matrix inversion equation composed of all single-station data

$$H = M\cdot\delta Q + E\cdot\delta\ln S + U\cdot\delta\ln P, \tag{13}$$

where H is a vector composed of residuals of logarithmic Pg spectra, δQ, $\delta\ln S$ and $\delta\ln P$ are all vectors composed of perturbations of Q, source and site responses, respectively, and are used to update them in iterations. M, E and U are coefficient matrices that establish the relationships between the observed single-station Pg-wave spectra and Q perturbations, source perturbations, and site response perturbations, respectively. Each row in matrix eq. (13) represents a single-station ray data. In a similar way, for two-station data, the matrix equation linking the residual of the spectral ratios and the perturbations of the model can be obtained from eq. (8), in which the source terms have been eliminated by taking spectral ratios,

$$H_{2sta} = M_{2sta}\cdot\delta Q + U_{2sta}\cdot\delta\ln P, \tag{14}$$

where H_{2sta} is a vector composed of residuals of logarithmic Pg spectral ratios, matrix M_{2sta} establishes the relationship between the Q perturbations and the residuals of Pg spectral ratios, matrix U_{2sta} establishes the relationship between perturbations of the site responses and the residuals of the Pg spectral ratios. Each row in eq. (14) represents a two-station spectral ratio data. As a trade-off, we used a two-step method to determine the effect of the site response. First, we temporarily neglected the site response terms by assuming $P_j(f) = 1$ and focused on inverting the source and attenuation measurements (e.g. Zhao *et al.* 2010). The site effects were left in the unsolved data residuals. After neglecting the site response term and combining eqs (13) and (14), we obtain an inversion system which jointly relates the residuals of single-station and two-station data with perturbations of the attenuations and source terms

$$\begin{bmatrix} H \\ H_{2sta}\end{bmatrix} = \begin{bmatrix} M \\ M_{2sta}\end{bmatrix}\cdot\delta Q + \begin{bmatrix} E \\ 0\end{bmatrix}\cdot\delta\ln S. \tag{15}$$

Eq. (15) can be solved using the least squares orthogonal factorization (LSQR) algorithm (Paige & Sanders 1982), and resulting perturbations are used to update the attenuation and source models in an iterative way. During the tomographic inversion, the target region was divided into $0.5^\circ \times 0.5^\circ$ cells. We used the regionally averaged Q_{Pg} model from two-station data as the initial model, which was calculated by averaging path Q values from all two station pairs throughout the entire study area. After 250 LSQR iterations, both the Q_{Pg} and source terms were ultimately obtained by minimizing the L2 norm of data residuals. The above inversions were independently conducted at 66 discrete frequencies between 0.05 and 20.0 Hz. Next, we invert the site responses from unresolved data residuals. During this, we require the overall effect of the network site response close to unity. This is equivalent to applying a constraint $\sum_j \ln[P_j] = 0$ (Ottemoller *et al.* 2002; Ottemöller 2002). To achieve this, the inversion is starting from initial values $P_j(f) = 1$, and at each iteration, a constraint $|\sum_j \delta\ln[P_j]| < \varepsilon$ is used, where ε is an empirical value for normalizing the site responses. The site responses of all stations ultimately obtained are shown in Fig. S2. After the inversion, the mean and standard deviations of data residuals corresponding to the best-fitting model are significantly reduced at all frequencies compared to those related to the initial model. As examples, illustrated in Fig. 4 are mean and standard deviations of data residuals before and after the inversion at 0.5, 1.0 and 5.0 Hz, in which the standard deviations are reduced from 1.68, 1.81 and 2.56 to 0.82, 0.84 and 0.94, respectively. Note that the residuals after inversion in Fig. 4 are the final results after further separating the site responses. Apparently, through the inversion, the error distributions become sharper and more unbiased. Next, we investigated the inverted Pg wave source spectra. Since inversions were independently conducted at individual frequencies, we have the source spectra $S(f)$ for all events. The seismic moment M_0 and the corner

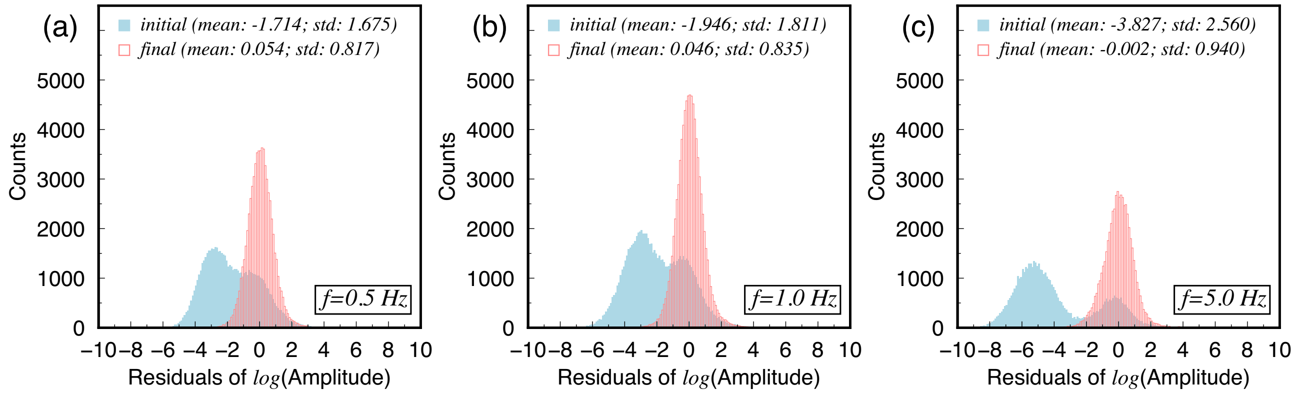

Figure 4. Residual histograms of Pg spectral amplitudes before (solid light blue) and after (hollow light red) inversions at 0.5, 1.0 and 5.0 Hz, respectively. In general, the inversions moved the means and residuals towards more unbiased and sharper distributions. The initial and final means and standard deviations are also labelled in the figure.

frequency f_c can be obtained by fitting the inverted source spectra with eq. (3). All obtained source parameters are listed in Table S1.

3.3 Checkerboard test

The resolution of the Q_{Pg} tomography was checked using the checkerboard test method. The checkerboard model was created by superimposing ± 7 per cent checkerboard Q perturbations on the initial Q model obtained from the two-station data at each frequency. The same single- and two-station rays as in the real data are used in the tests. Dense rays cover almost the entire study area, except at the western and southern edges, which are covered by relatively sparse two-station rays. Fig. 5 illustrates single-station rays, two-station rays, and recovered checkerboard models at 0.5, 1.0 and 5.0 Hz, respectively. The results demonstrated the resolution can approach approximately $0.5^{\circ} \times 0.5^{\circ}$ or higher over most of the study area.

4 RESULTS

Based on the data set and the processing method described in previous sections, we obtained a broad-band Pg-wave attenuation model for the crust in SE Tibet. The model is composed of Q_{Pg} distributions at 66 individual frequencies between 0.05 and 20 Hz.

4.1 Q_{Pg} maps at discrete frequencies

As examples, Fig. 6 illustrates the Q_{Pg} distributions at 0.5, 1.0 and 5.0 Hz, respectively, with a resolution of $0.5^{\circ} \times 0.5^{\circ}$. In general, the Q_{Pg} values dominantly increase with increasing frequency, but show similar attenuation patterns at different frequencies. The average Q_0 (Q_{Pg} at 1 Hz) in the entire study area is 186, with its logarithmic standard deviations corresponding to 108 and 320 (Table 1). The results reveal that there are two major low-Q_{Pg} zones with $Q_0 = 147$ (90–241) in the Songpan-Ganzi Block and Western Sichuan Block (LQZ1) and $Q_0 = 100$ (57–175) at the junction among the Yangtze plate, the Central Yunnan block, and the Indo-China block (LQZ2) with an approximately NE−SW distribution. Between LQZ1 and LQZ2 is the Emeishan large igneous province (ELIP), which is characterized by high Q_{Pg} values. The Sichuan Basin (SB) also features high Q_{Pg} values because of its old and stable terrane characteristics (Yang *et al.* 2021b). Pg attenuation is generally strong in areas with intense tectonic activities but relatively weak in stable rigid blocks (Singh *et al.* 2011). Our results are consistent with previously published Pg attenuation results in the eastern Tibetan Plateau (Bao *et al.* 2011b).

4.2 Broad-band Q_{Pg} map

Our Pg-wave attenuation tomography was conducted independently at individual frequencies without applying any a priori constraints on its frequency dependency. Therefore, the resulting model can be used to further investigate its frequency property, similar to the previous investigation on the Lg-wave attenuation (Benz *et al.* 1997; Pasyanos *et al.* 2009b; Zhao & Mousavi 2018; He *et al.* 2021). We used the statistical method to explore the Q_{Pg} frequency dependence. Figs 7(a)–(e) illustrate Q_{Pg} variations versus the frequency in selected geological units and blocks, including low-Q_{Pg} zones, LQZ1 and LQZ2 and relatively high-Q_{Pg} zones, the core of the ELIP, the SB and the Youjiang Basin (YJB). The grey crosses are directly inverted Q_{Pg} values at grid points within each targeted area. Color squares and error bars are mean values and standard deviations at 66 discrete frequencies. Fig. 7(f) compares frequency-dependencies for all blocks, including the SB, the core of the ELIP, the Yangtze Block (YZ), the YJB, the Three-River Orogenic Belt (TRB), the Indo-China Block (ICB), the Central Yunnan Block (CYB), the Western Sichuan Block (WSB), the Songpan-Ganzi Block (SGB), LQZ1 and LQZ2. The block names are labelled in the panels and all Q_{Pg} values are also listed in Table 1. At the low-frequency end, the Q_{Pg} values generally increase from 0.05 to 0.2 Hz and slightly decrease from 0.2 to 0.5 Hz. At higher frequencies, Q_{Pg} values increase again, with a moderate slope between 0.5 and 5.0 Hz and a steeper slope from 5.0 to 20.0 Hz. The peak around 0.2 Hz may be partially affected by the low-frequency noise or Rayleigh-wave energy. The Q_{Pg} values between 0.5 and 5.0 Hz are more sensitive to the properties of different geological blocks. Thus, we used the broad-band Q_{Pg} image, obtained by averaging the Q_{Pg} between 0.5 and 5.0 Hz, to characterize the crustal Pg attenuation in the study area (Fig. 8a).

Broad-band Q_{Pg} map (Fig. 8a) exhibits two isolated strong Pg attenuation zones, LQZ1 and LQZ2, and two weak Pg attenuation areas, the SB and the inner zone of the ELIP. The broad-band Q_{Pg} attenuation is also compared with broad-band Q_{Lg} between 0.3 and 5.0 Hz in Fig. 8(b) (He *et al.* 2021), the *Vp* distribution at 20 km depth in Fig. 8(c) (Liu *et al.* 2021), and the *Vs* distribution at 22.5 km in Fig. 8(d) (Bao *et al.* 2015). These maps show good consistencies

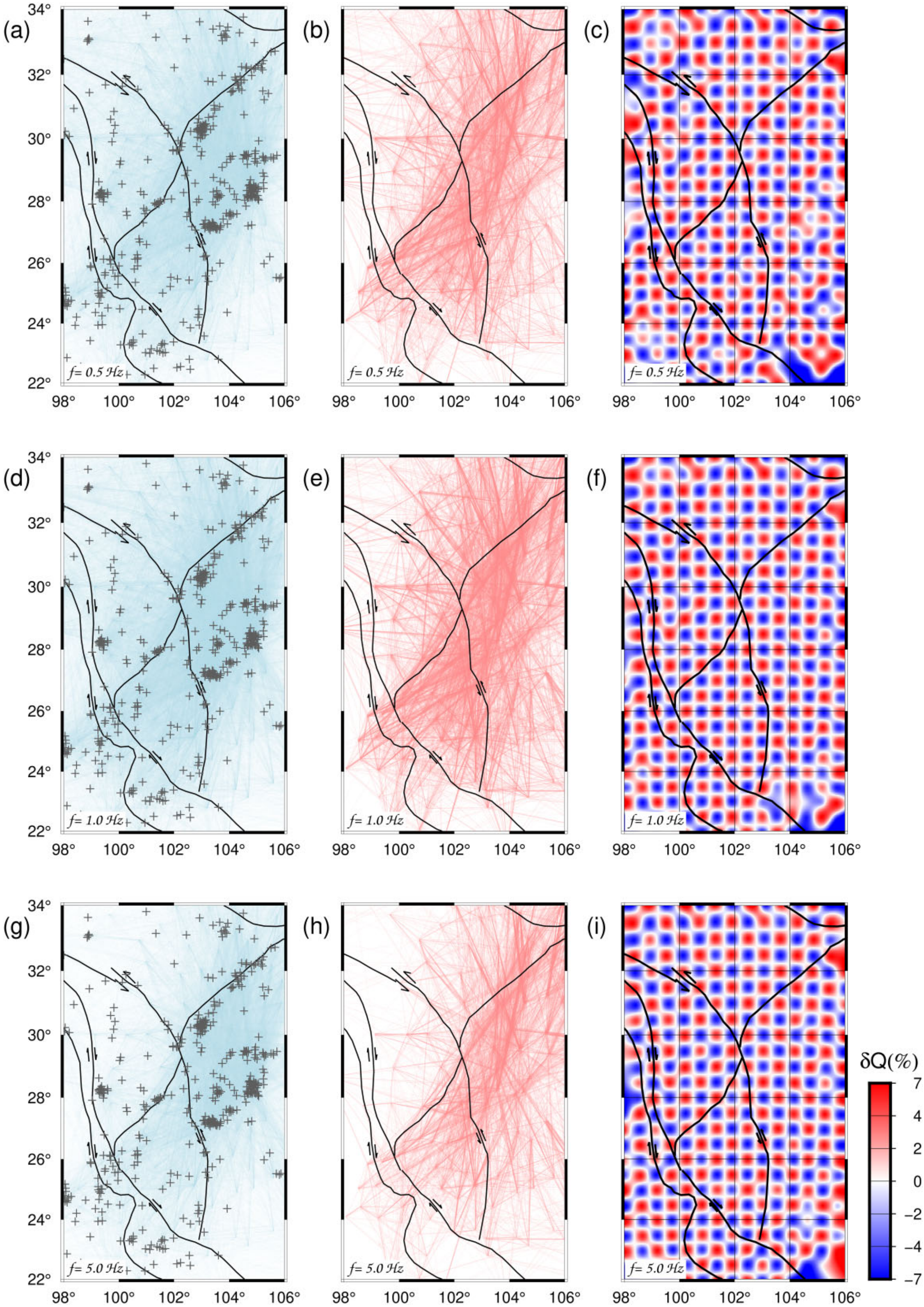

Figure 5. Maps of the single-station (left-hand column) and two-station data (centre column) ray coverage, and recovered checkerboard models (right-hand column) at 0.5 Hz (top row), 1.0 Hz (middle row) and 5.0 Hz (bottom row), respectively. Additionally, fault systems (black lines) and earthquake epicentres (dark grey crosses) are overlaid on these maps.

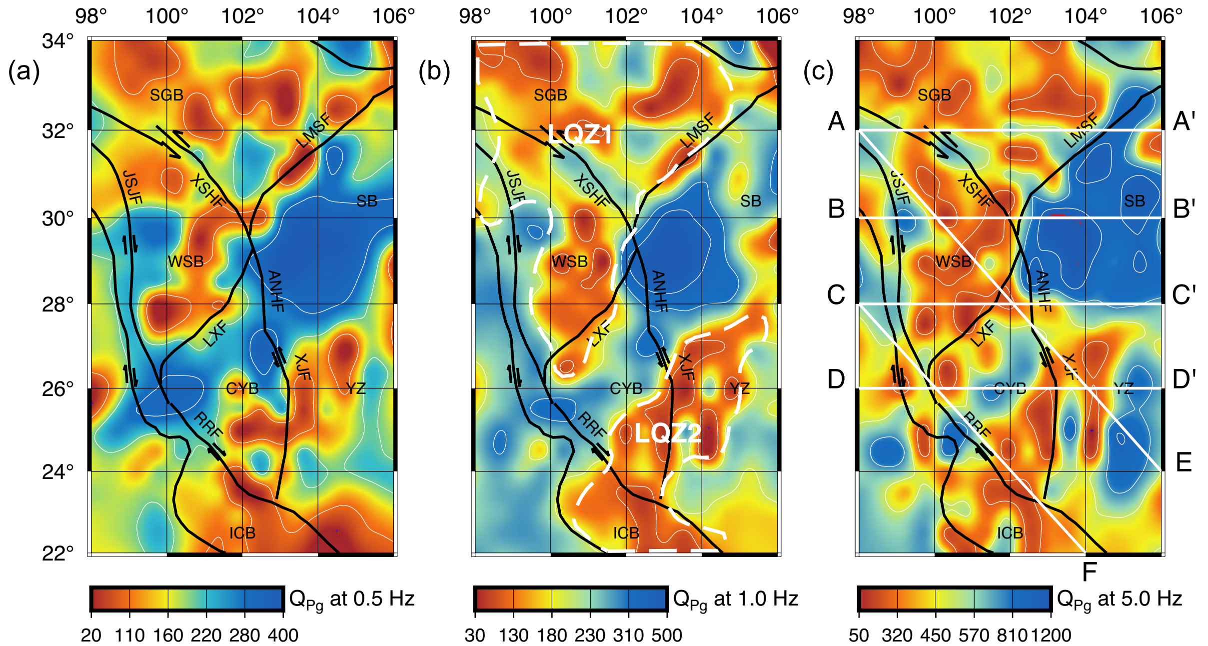

Figure 6. (a)–(c) Selected Q_{Pg} maps at 0.5, 1.0 and 5.0 Hz, in which the major faults and geological blocks are labelled. Note, different colour scales are used for different frequencies. The two low-Q zones, LQZ1 and LQZ2, are delineated by white dashed lines in (b). The locations of the profiles in Fig. 9 are marked in (c) with white lines. The abbreviations are the same as those used in Fig. 1.

Table 1. Q_{Pg} for individual geological blocks.

Geological block	Abbreviation	Single- plus two-station data			Two-station data		CRUST1.0*	
		Average Q between 0.5–5.0 Hz (Q_{low}-Q_{high})	Frequency dependence η (0.5–5.0 Hz)	1.0 Hz Q (Q_{low}-Q_{high})	Average Q between 0.5–5.0 Hz (Q_{low}-Q_{high})	1.0 Hz Q (Q_{low}-Q_{high})	Crustal thickness (km)	Sediment thickness (km)
Low-Q zone 1	LQZ1	181 (108–302)	0.35 ± 0.02	147 (90–241)	178 (93–340)	141 (59–336)	60.35 ± 6.29	0.01 ± 0.04
Low-Q zone 2	LQZ2	142 (78–259)	0.50 ± 0.05	100 (57–175)	164 (78–346)	104 (36–294)	40.55 ± 5.18	2.01 ± 2.68
Emeishan Large Igneous Province	ELIP	336 (229–493)	0.37 ± 0.07	268 (230–314)	355 (212–594)	301 (181–502)	49.20 ± 0.95	0.73 ± 1.10
Central Yunnan Block	CYB	226 (129–397)	0.33 ± 0.04	184 (118–286)	215 (98–471)	168 (60–469)	47.12 ± 4.44	0.50 ± 0.75
Indo-China Block	ICB	235 (137–403)	0.40 ± 0.04	190 (124–291)	184 (110–310)	141 (81–245)	34.45 ± 2.05	0.14 ± 0.12
Three-River Orogenic Belt	TRB	264 (172–406)	0.32 ± 0.03	240 (193–298)	235 (148–372)	182 (98–337)	49.58 ± 12.54	0.05 ± 0.06
Sichuan Basin	SB	395 (224–699)	0.58 ± 0.06	270 (177–411)	380 (202–712)	239 (114–501)	43.83 ± 3.34	6.57 ± 1.40
Songpan-Ganzi Block	SGB	199 (110–359)	0.46 ± 0.03	147 (79–271)	202 (97–422)	155 (69–344)	58.73 ± 7.81	0.02 ± 0.05
Western Sichuan Block	WSB	202 (121–335)	0.29 ± 0.03	168 (101–280)	192 (109–336)	155 (66–363)	61.41 ± 4.05	0.00 ± 0.00
Youjiang Basin	YJB	284 (157–513)	0.67 ± 0.07	192 (128–287)	265 (158–445)	203 (153–268)	37.81 ± 2.93	1.00 ± 1.73
Yangtze Block	YZ	261 (134–510)	0.50 ± 0.04	190 (93–387)	287 (137–599)	199 (71–560)	46.20 ± 3.15	4.37 ± 2.79
Entire study region	ALL	240 (131–440)	0.44 ± 0.01	186 (108–320)	236 (120–464)	177 (80–395)	49.15 ± 10.71	1.41 ± 2.54

†Q_{low} and Q_{high} are average Q minus or plus standard deviation in the logarithmic scale, respectively.
*From Laske *et al.* (2013).

among anomalies from independent observations in the crust of SE Tibet. For example, low Q_{Pg} values correlate well with low Q_{Lg}, low Vp and low Vs values in LQZ1 and LQZ2, whereas high Q_{Pg} values correspond to high Q_{Lg}, high Vp and high Vs values in stable areas such as the SB and central CYB. The correlation between Q_{Pg} and Q_{Lg} (He *et al.* 2021) shows that the *P*- and *S*-wave attenuation structures in the crust in SE Tibet are generally consistent, although some differences lie in the inner zone of the ELIP (longitude 101–103° and latitude 25.5–27.5°), where it is characterized by slightly higher Q_{Pg} but relatively low Q_{Lg} (Fig. 8). The Q_{Lg} pattern may indicate a complicated connection for the crustal material flow (He *et al.* 2021). On the contrary, in our Pg-wave Q map, high Q_{Pg} anomalies appear in the inner zone of the ELIP, which may reflect that the mantle plume invaded and strengthened the crust in the

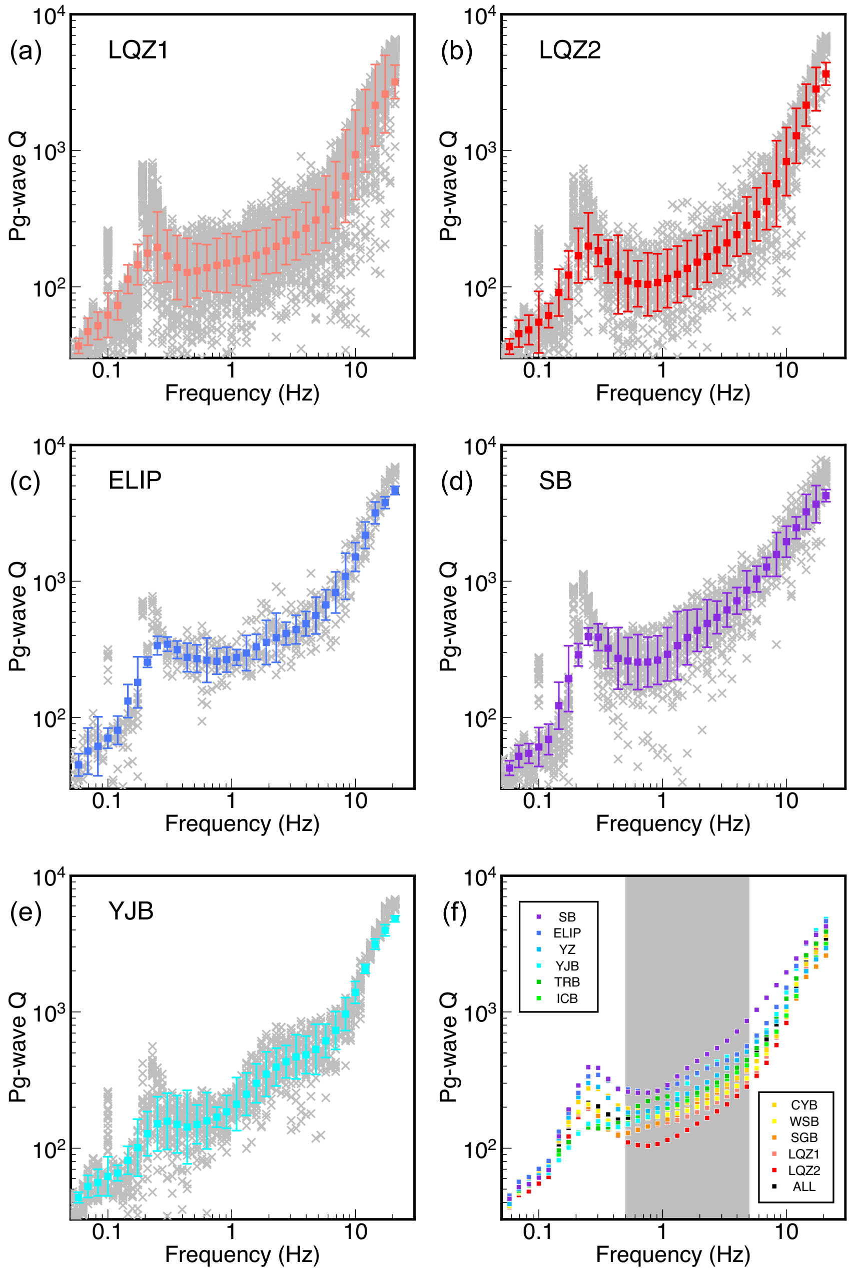

Figure 7. (a)–(e) The frequency-dependent $Q_{\rm Pg}$ for selected geological blocks, where the grey crosses are directly inverted $Q_{\rm Pg}$ values, colour squares and error bars are their mean values and standard deviations at different frequencies. (f) Summary of frequency-dependent $Q_{\rm Pg}$ for all blocks. The block names are labelled in the panels and these $Q_{\rm Pg}$ values are also listed in Table 1.

region (Xu *et al.* 2004; Zhao *et al.* 2020), thus making LQZ1 and LQZ2 disconnected. We will further discuss this in Sections 5.2 and 5.3.

The widely used power-law Q model, $Q(f) = Q_0 \cdot f^{\eta}$, where Q_0 is the 1 Hz Q and η is the frequency-dependence coefficient, is obtained by applying a priori power-law frequency dependency to the data. It's apparently oversimplified the complex frequency dependency over a broad frequency band (Fig. 7). However, within a relatively narrow frequency band, for example between 0.5 and 5.0 Hz, the power-law model may be useful to characterize the frequency dependency. Thus, by fitting the power-law model within this frequency band, we obtained both Q_0 and the exponent η for different geological blocks (Table 1). The Q_0 values are lower, 147 in LQZ1 and 100 in LQZ2, than those in stable areas, 270 in SB, and 268 in the core of the ELIP (Table 1). The exponents η vary from 0.29 to 0.67. The $Q_{\rm Pg}$ values are likely dependent upon the tectonic activities in the southeastern margin of the Tibetan Plateau and surrounding areas (Table 1; Bao *et al.* 2011b).

4.3 Frequency-dependent $Q_{\rm Pg}$ cross-sections

To further investigate relations among different observations, Fig. 9 illustrates six comprehensive cross-sections including surface to-

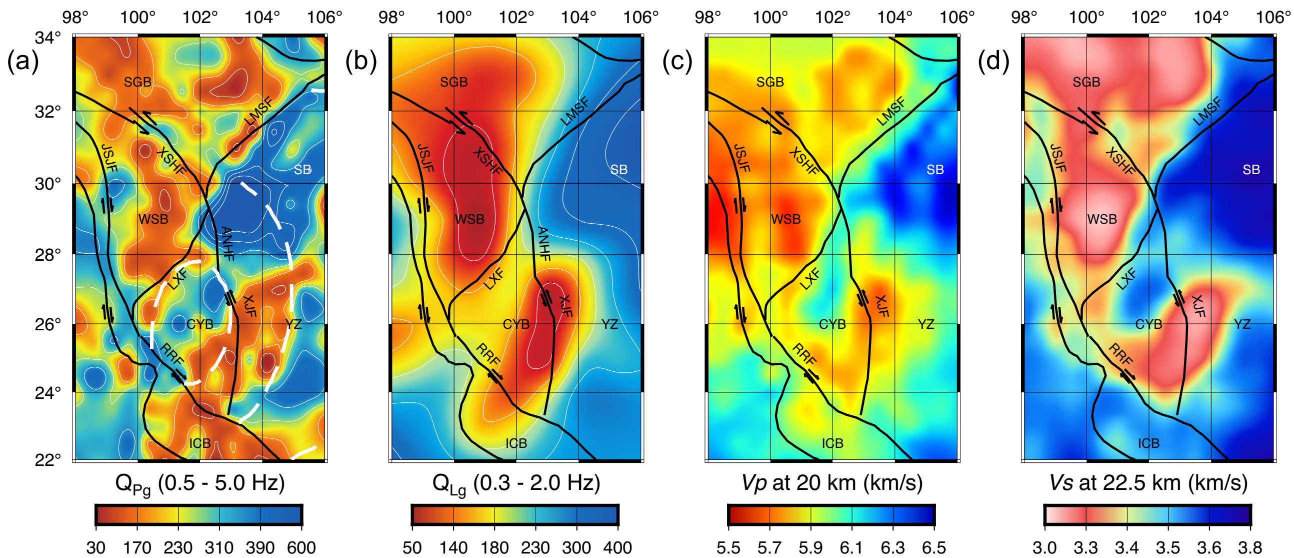

Figure 8. Comparisons among Q_{Pg}, Q_{Lg}, *Vp* and *Vs* maps in SE Tibet, with (a) the broad-band Q_{Pg} (0.5–5.0 Hz; this study), (b) broad-band Q_{Lg} (0.3–2.0 Hz; He *et al.* 2021), (c) *Vp* at 20 km depth (Liu *et al.* 2021) and (d) *Vs* at 22.5 km depth (Bao *et al.* 2015). The major faults and geological blocks are labelled in these maps. White dashed lines divide the Emeishan large igneous province into its inner, intermediate and outer zones. The abbreviations are the same as those used in Fig. 1.

pography, *Vs* versus depth (Bao *et al.* 2015), Moho depth (Laske *et al.* 2013) and Q_{Pg} versus frequency obtained in this study. The surface locations of these profiles are shown in Fig. 6(c). Profiles A–A' along 32°N (Fig. 9a) and B–B' along 30°N (Fig. 9b) are both running from the high-elevation Tibetan Plateau in the west to the low-elevation foreland in the east. Low-Q_{Pg} anomalies between 0.3 and 10.0 Hz beneath the LQZ1 are located to the west of the Longmenshan Fault (LMSF). The LQZ1 also features low-*Vs* anomalies, possibly revealing a partially-melted weak crust in SE Tibet. The SB, characterized by high Q_{Pg} values, is a stable continental block with thick lithospheric roots (Yang *et al.* 2021b). The LMSF is a clear rheological boundary between the soft LQZ1 and the hard SB. Low-Q_{Pg} anomalies at around 10.0 Hz correlate to the shallow low-*Vs* anomalies beneath the SB, and are likely due to strong high-frequency attenuations in the thick sedimentary layer. Profiles C–C' along 28°N (Fig. 9c) and D–D' along 26°N (Fig. 9d) are both passing through LQZ1 and LQZ2 from west to east, where the two LQZs are separated by a high-Q_{Pg} and high-velocity anomaly beneath the CYB, as shown by the white box in Fig. 9(d). This high-Q_{Pg} and high-velocity region is also coincident with the core of the ELIP, which is generally interpreted as mafic magmatic underplating by previous studies (Zhao *et al.* 2020).

5 DISCUSSIONS

5.1 Comparison between Q_0 values obtained from the single and two-station methods

In this study, we developed a Pg-wave attenuation tomography method by combining both the single- and two-station data. The two-station method has the advantage that the source term can be eliminated from the data. Hence, the trade-off between the source and attenuation can be effectively eliminated. The two-station method has been widely used in constructing attenuation models for different wave types (Xie *et al.* 2004; Bao *et al.* 2011a; Gallegos *et al.* 2017; Singh *et al.* 2019). However, limited by their geometrical locations, the two-station data usually generate low inversion resolutions due to their availability. The joint inversion method using both the single- and two-station data proposed in this study can greatly increase the data coverage; not only improve the inversion resolution, but also reasonably reduce the trade-offs among the attenuation, the source terms, and the site responses (e.g. Zhao *et al.* 2013; Zhao & Xie 2016). If using the two-station method alone, the source radiation pattern issue can be neglected. However, including the single-station data in the inversion will involve the source radiation pattern. We replaced the radiation pattern with an average value and neglected their angle dependence in the Q_{Pg} tomography. This is based on the below considerations. First, the Pg waveforms extracted from a group velocity window consist of the interferences of numerous arrivals, in which both the P wave propagating within granite, other reverberations and converted waves in the crust are involved (Langston 1982; Campillo *et al.* 1984). Secondly, the radiation pattern is gradually distorted and altered from the original four-lobe shape with increasing frequency and epicentral distance (Kobayashi *et al.* 2015). The effect of epicentral distance on the radiation pattern is dominant when the epicentral distance is greater than 100 km (Wang *et al.* 2021). As the frequency increases above 1 Hz, the radiation pattern gradually changes from certainty to randomness (Pitarka *et al.* 2000). When the frequency and the epicentral distance are both large, the radiation coefficients in the two horizontal directions can take a uniform value, and the radiation pattern is completely distorted (Wang *et al.* 2021). In this case, the average radiation pattern coefficient was generally adopted for both *P* and *S* waves (Pasyanos *et al.* 2009a; Kwiatek *et al.* 2019), and hence, the source radiation pattern can be reasonably ignored. Additionally, the geometrical spreading of Pg waves is independent of the source mechanism based on the theoretical seismograms of regional crustal phases (Campillo *et al.* 1984).

To illustrate the reliability of the proposed Pg attenuation tomography, we investigate the average Q_{Pg} values calculated from both the single- and two-station method and the two-station method. Fig. 10 shows the average Q_{Pg} from the single- and two-station method versus those from the two-station only method, for

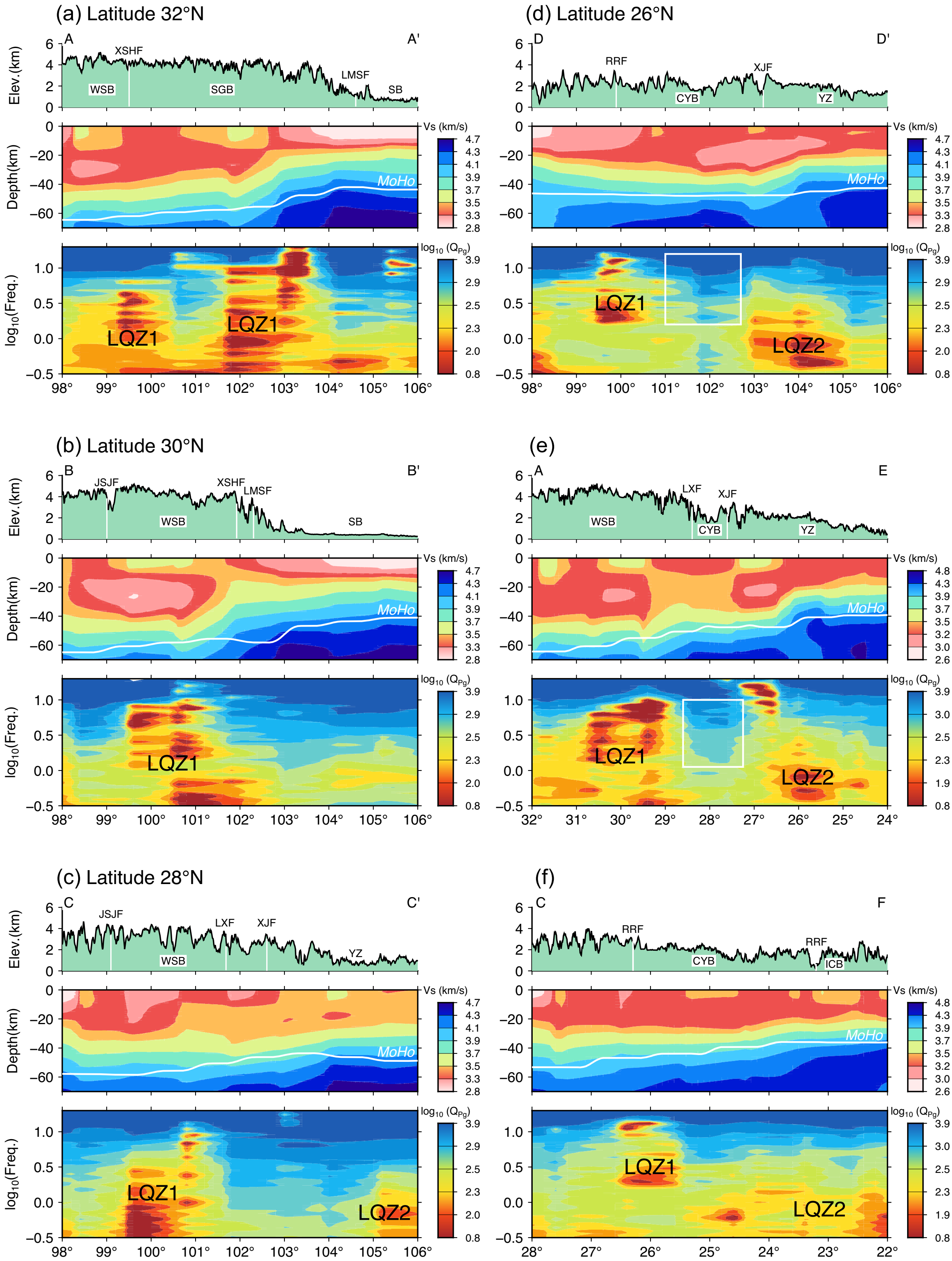

Figure 9. Comparisons of profiles among the surface topography, shear velocity *Vs* (Bao *et al.* 2015), Moho depth (white lines in middle panel), and Q_{Pg} versus the frequency, where the major faults and blocks are labelled. The surface locations of these profiles are illustrated in Fig. 6(c). The abbreviations for the geological blocks are similar to those used in Fig. 1. The locations of the core of the ELIP are highlighted by white rectangles.

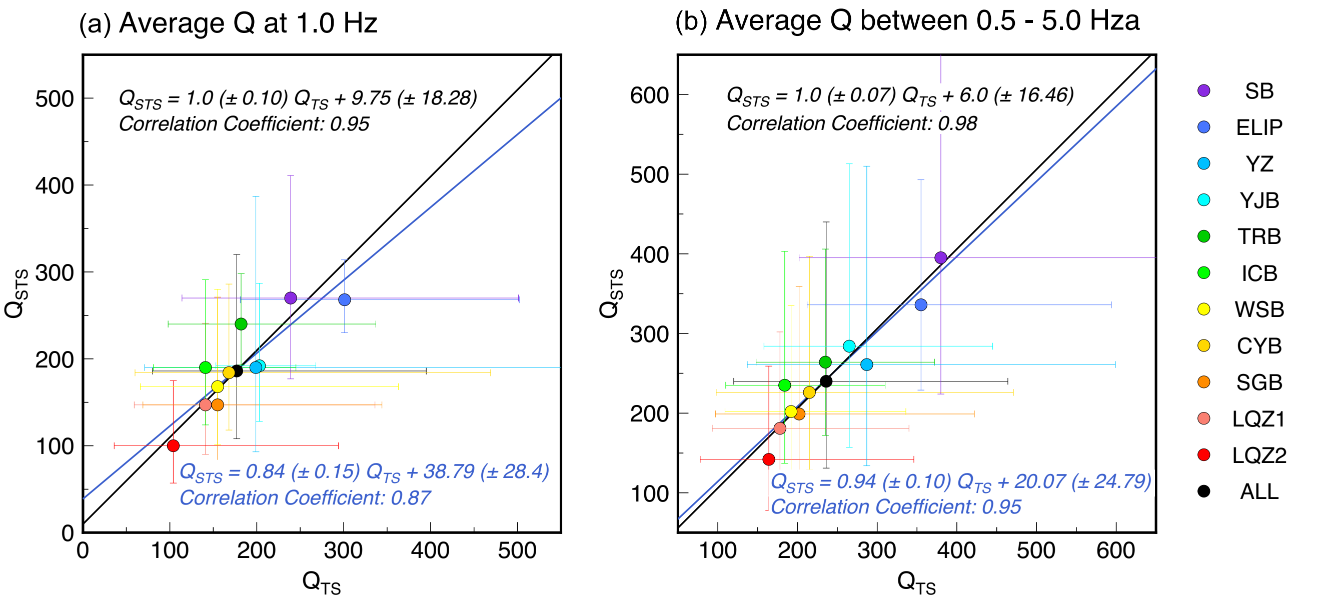

Figure 10. Comparison between the Q_{Pg} values obtained using combined single- and two-station data (Q_{STS}) and those from the two-station data only (Q_{TS}). (a) Average 1 Hz Q_{STS} values versus those of the Q_{TS} for different geological blocks. (b) Average Q_{STS} values between 0.5 and 5.0 Hz versus those from the Q_{TS} for different geological blocks. The circles and their error bars show the Q_{Pg} values and their standard deviations (refer to Table 1). Different colours denote individual geological blocks as shown on the right. The blue lines are their linear regressions, and the black lines are linear fits with their slopes fixed to unity. The corresponding correlation coefficients are also labelled.

individual geological blocks at 1.0 Hz and between 0.5 and 5.0 Hz band, respectively. Through linear regressions, the slopes were 0.84 (±0.15) at 1.0 Hz and 0.94 (±0.1) at 0.5–5.0 Hz, respectively, both closing to 1. When we fix the slopes to the unity, the Q intercepts were 9.75 (±18.28) and 6.0 (±16.46) for Q_{Pg} at 1.0 Hz and between 0.5 and 5.0 Hz. The corresponding correlation coefficients were 0.95 and 0.98, respectively. This means that the Q_{Pg} values of different geological blocks obtained by these two methods are highly correlated, although the combined single- and two-station data give much higher resolution. For the entire study area, we obtained average Q_{Pg} values of 186 (108–320) at 1.0 Hz and 240 (131–440) between 0.5 and 5.0 Hz by using single- and two-station methods, and these values are 177 (80–395) and 236 (120–464) obtained using the two-station method (Table 1). We also inverted a broad-band Q_{Pg} map using the two-station method (Fig. S3) and found that it is similar to the main pattern of our broad-band Q_{Pg} model obtained by the single- and two-station method. In summary, the Q_{Pg} values obtained using our method are highly correlated with those obtained using the two-station method, which demonstrates that the source radiation pattern has little influence on the results.

5.2 the lack of connection between the two low-Q_{Pg} zones in SE Tibet

To explore the crustal material transportation patterns in SE Tibet, we investigated the spatial extension of strong Pg attenuation zones and the connectivity of these zones. Based on high-density data, we revealed two isolated mechanically weak zones with low Q_{Pg}, which are separated by the high-Q_{Pg} CYB in the crust (Figs 6 and 8).

In general, our broad-band Pg attenuation pattern is similar to the Lg attenuation distribution, but in the crust beneath the CYB, there are high Q_{Pg} values and relatively low Q_{Lg} values (longitude 101–103° and latitude 25.5–27.5° in Figs 8a and b) (He *et al.* 2021). This discrepancy may result from the variability in Pg and Lg propagation paths, and their specific sampling depths are also not identical. Lg wave is known to be a fairly robust seismic phase sampling the whole crust (Kennett 1989). While we mainly use secondary Pg waves with epicentral distances beyond the crossover distance, they are composed of interferences of numerous arrivals, and their depth sampling in the crust is unclear. Although Pg waves at large distances are composed of reverberations in the whole crust, some studies have indicated the importance of shallow low-velocity zones in promoting large-distance propagation. For instance, it is difficult to sustain the Pg phase to even 500 km without the existence of a low-velocity zone near the surface (Kennett 1989). Steck *et al.* (2011) obtained velocity images of the western United States by inverting the Pg phase travel times and demonstrated that they mainly reflect the velocity structure of the middle to upper crust via a series of comparisons, although the influence of the whole-crust reverberations cannot be ruled out. Therefore, we believe that our images reflect the characteristics of the whole crust, but the upper to middle crust depth may account for a large weight. In Figs 8(c) and (d), our broad-band map is consistent well with the *P*-wave velocity at 20 km depth from Liu *et al.* (2021) and the *S*-wave velocity at 22.5 km depth from Bao *et al.* (2015) (low Q with low velocities and vice versa), which supports this point to some extent. Thus, the inconsistency between the Q_{Pg} and Q_{Lg} images may imply weak connections in the deeper crust beneath the CYB. To reconcile these observations, we conclude that our results reveal two mutually independent strong attenuation zones in the crust, but we do not rule out the possibility of weak connections in the deep lower crust.

5.3 Crustal flow restricted and stopped in the Western Sichuan block

Analysing the origin of the strong attenuation zones is crucial to understand the tectonic evolution of SE Tibet. Previous studies have observed that the crust of the southeastern Tibetan Plateau has a series of geophysical anomalies, including low shear-wave velocity (Liu *et al.* 2014; Bao *et al.* 2015), high electrical conductivity (Bai *et al.* 2010; Li *et al.* 2020), strong Lg-wave attenuation (Zhao *et al.* 2013), high Poisson's ratios (Sun *et al.* 2012) and high heat flow (Jiang *et al.* 2019). These anomalies are spatially consistent with the strong attenuation zone beneath the Songpan-Ganzi Block and the Western Sichuan Block in our results. All these are commonly attributed to the presence of aqueous fluids or partial melting (Yao *et al.* 2008; Caldwell *et al.* 2009; Bai *et al.* 2010). Our results support this point of view, as strong seismic wave attenuation is usually an indication of the presence of aqueous fluids, fracture zones, and partial melting associated with high temperatures (Winkler & Nur 1982; Kong *et al.* 2013; Amalokwu *et al.* 2014). Increased fluid content or a 5 per cent melt can reduce the viscosity of crustal rocks by an order of magnitude, thus making it possible for the mid-lower crustal materials to flow (Rosenberg & Handy 2005). Accordingly, some of the studies support the previously proposed mid-lower crustal flow model (Royden *et al.* 1997; Clark & Royden 2000) to explain crustal escape and speculate that the geophysical anomalies observed in SE Tibet correspond to potential crustal flow channels. The magnetotelluric imaging of Bai *et al.* (2010) revealed two high electrical conductivity channels at depths of 20–40 km in SE Tibet. The images based on Rayleigh-wave dispersion and receiver functions depict two low-velocity channels around the EHS with depths of 10–20 km and 20–30 km (Bao *et al.* 2015). Despite minor differences, the LQZ1 beneath the WSB coincides with the curved segment of the right branch of the high electrical conductivity channel (Bai *et al.* 2010) and low-velocity channel A (Bao *et al.* 2015). Fig. 9 shows that LQZ1 is closely related to low-velocity anomalies, crustal thickening, and an increase in surface elevation. These results are consistent with the viewpoint that the accumulation of crustal flow leads to crustal thickening, as proposed by the crustal channel flow model (Royden *et al.* 1997; Clark & Royden 2000). Therefore, we suggest that the low-Q_{Pg} anomalies beneath the WSB serve as mechanically weak crustal flow channels, possibly with aqueous fluids or partial melting.

A high-Q_{Pg} anomaly appears in the middle of the CYB, corresponding to the inner zone of the ELIP. Together with the high-Q_{Pg} SB, it separates two strong attenuation zones in the crust of SE Tibet (Fig. 9). The ELIP is a large igneous rock region generated by mantle plumes (Chung & Jahn 1995; Xu *et al.* 2004; Zhang *et al.* 2008), with a formation time of approximately 260 Ma (Shellnutt *et al.* 2008). According to the degree of denudation, the entire ELIP is divided into the inner, middle and outer zones from west to east. The inner zone is characterized by high velocities (Yao *et al.* 2008; Liu *et al.* 2014), high densities (Deng *et al.* 2014), high resistivities (Li *et al.* 2020) and weak azimuthal anisotropy (Li *et al.* 2021), and is interpreted as mafic underplating formed by a cooled basaltic magma chamber caused by Permian mantle plume activities (He *et al.* 2003; Chen *et al.* 2015; Zhao *et al.* 2020). The early upwelling of the mantle plume beneath the inner zone strengthened the lithosphere of the CYB, as revealed by the strong vertically orientated anisotropy (Li *et al.* 2021), and formed a rigid barrier at the lithospheric scale on the western edge of the Tibetan Plateau. Therefore, we suggest that the southeastward expansion of the mid-lower crustal material flow through the LQZ1 channel was blocked by the pre-existing mafic magma remnants in the inner zone of the ELIP and gradually accumulated to form significant crustal thickening and surface uplift in the Western Sichuan Block.

LQZ2 is a strong attenuation zone near the Xiaojiang Fault and Red River Fault, where the crust is characterized by low shear-wave velocities (Qiao *et al.* 2018; Zhang *et al.* 2020), high electrical conductivity (Bai *et al.* 2010), high Poisson's ratios (Sun *et al.* 2014) and strong Lg-wave attenuation (Zhao *et al.* 2013). LQZ2 may not connect with the crustal flow channels in the Tibetan Plateau for the following reasons: (1) LQZ1 and LQZ2 are not connected, instead, they are isolated from each other; thus, mid-lower crustal materials are unlikely to flow into the Yangtze Craton under the blockage formed by the ELIP. (2) The Moho and surface topography of LQZ2 vary gently, without significant crustal thickening and elevation increases as those observed from LQZ1 (Figs 9c–f). This is inconsistent with the classic crustal flow model (Royden *et al.* 1997; Clark & Royden 2000). In addition, the observed surface uplift speed reveals significant surface subsidence in LQZ1, whereas positive uplift is dominated in LQZ2 with the uplift rate ranging between 1.0 and 2.0 mm yr^{-1} (Wu *et al.* 2022). The NE−SW fast velocity directions at depths of 25 and 40 km below the Xiaojiang fault zone are inconsistent with the overall trend of material extrusion towards the southeast (Huang *et al.* 2018; Han *et al.* 2022). Therefore, the mid-lower crustal material flow in SE Tibet is likely truncated by the strengthened crust and mafic remnants in the ELIP inner zone, and is confined in the WSB without extending further southeastward.

5.4 Asthenospheric upwelling near the Red River and Xiaojiang Faults

In previous sections, we have demonstrated that LQZ2 is not derived from mid-lower crust channel flow because it is not connected to LQZ1, the gentle changes in the surface elevation and Moho, and the NE−SW fast velocity directions in the mid-lower crust are inconsistent with the material extrusion direction (Huang *et al.* 2018; Han *et al.* 2022). Some recent observations indicated that LQZ2 is likely related to the local upwelling of thermal mantle materials. For example, low shear-wave velocity anomalies were observed in the middle crust (Qiao *et al.* 2018), and low *P*- and *S*-wave velocities also appear in the upper mantle in LQZ2 (Huang *et al.* 2015; Zhang *et al.* 2020). High conductivity values within the crust of the Chuxiong Basin, south of the CYB, were observed based on magnetotelluric results, which is difficult to explain with partial melts alone and may require a sustained supply of saline aqueous fluids (Li *et al.* 2020). Yu *et al.* (2020) observed the existence of large low-resistivity bodies in the crust below the Red River Fault and the upper mantle on the northeastern side of the Red River Fault based on a 3-D magnetotelluric method. They were interpreted as partial melts in the upper mantle. In SE Tibet, to the south of 26°20′N, the azimuthal anisotropy changes sharply from north–south to strongly east–west at the top of the upper mantle beneath LQZ2 (Gao *et al.* 2020), which may be related to the directional flow of hot materials. Lei *et al.* (2019) suggested that mantle upwelling may be caused by the deep subduction, stagnancy, and dehydration of the Indian slab.

Because the Red River Fault cuts through the whole crust and the Xiaojiang Fault is a deeply penetrating and tectonically active fault zone (Zhao *et al.* 2020), asthenospheric upwelling is likely to enter the crust along the Red River Fault and Xiaojiang Fault (Chung *et al.* 1998). This is consistent with the geochemical observations. For example, many components of alkaline intrusions exposed around the Red River shear zone originate from enriched mantle sources (Zhang & Xie 1997; Bi *et al.* 2009). A series of large Au-rich deposits exist on the western edge of the Yangtze Craton, near the Red River shear zone (Liu *et al.* 2015; Gao *et al.* 2018). By analysing the elements and zircon isotopes of the xenoliths, Hou *et al.* (2017) found that the formation mechanism of these Au-rich porphyry deposits is related to the reactivation of cratonic edges, triggered by mafic ultrapotassic melts invading from the mantle into the crust. Both the U-Pb and Rb-Sr dating and Pb-Sr-Nd isotope tracing reveal that along the Red River shear zone, the mantle magma successively migrated into the crust, inducing anatectic melting at 20–15 km depth (Zhang & Schärer 1999). Our strong Pg attenuation in the LQZ2, together with these geophysical and geochemical observations, indicates that the crust beneath the Xiaojiang Fault and Red River Fault may be affected by the upwelling of hot mantle material along these faults that cut the entire crust.

5.5 Implications for crustal tectonic escape in Southeastern Tibet

Some classic end-member models, such as the rigid-block extrusion model (Molnar & Tapponnier 1975) and the mid-lower crustal channel flow model (Royden *et al.* 1997), have been proposed to explain the crustal thickening and material escape on the southeastern margin of the Tibetan Plateau caused by the collision between the Indian Plate and the Eurasian Plate since 55 Ma. The existence of crustal flow in this region is supported by some geophysical observations to a certain extent, such as low seismic wave velocities (Liu *et al.* 2014; Bao *et al.* 2015), strong Lg-wave attenuation (Zhao *et al.* 2013), high electrical conductivity (Bai *et al.* 2010; Li *et al.* 2020), high heat flow (Hu *et al.* 2000; Jiang *et al.* 2019) and other intracrustal features. Analysis of the slip of the fault system since 4 Ma indicates that the crustal material east of the EHS is dominated by extensional structures and lacks crustal shortening, which closely resembles the kinematic interpretation of the crustal flow model (Wang *et al.* 1998). A 3-D finite element simulation demonstrated that the present-day crustal deformation in SE Tibet can hardly be explained solely by the tectonic extrusion, instead, it is more likely driven by the gravitational spreading of the uplifted plateau material (Li *et al.* 2019). The gravitational spreading model is similar to the crustal flow model when the pressure gradient driving the crustal flow comes from the topographic gradient. High-precision uplift data of the Tibetan Plateau indicate that the widely distributed surface subsidence of SE Tibet is a consequence of crustal flow and gravitational collapse (Wu *et al.* 2022). The lack of strong radial anisotropy in the mid-lower crust of this region calls into question the large-scale directional crustal flow, and the flow is likely to be small in scale, inhomogeneous, and disordered (Bao *et al.* 2020). The ductile lower-crustal materials may couple with the ductile uppermost mantle and move together, which conversely challenges the view that the ductile lower-crustal material cannot flow because it is strongly coupled with the underlying lithosphere (Chen & Gerya 2016).

Thermochronological studies indicated that large regions of eastern Tibet may have attained significant elevation before the Late Miocene, further indicating that crustal thickening in the Sichuan Basin during the Oligocene cannot be easily attributed to lower crustal flow (Wang *et al.* 2012). This is because the timescale required for the thermal weakening of the thickened crust to reach an effective viscosity allowing crustal flow is 20 Myr (Beaumont *et al.* 2004). Since the Late Miocene, SE Tibet has experienced rapid uplift (Clark *et al.* 2005), after which gravity collapse served as the dominant factor driving crustal extension (Xu *et al.* 2020); the growth of the plateau during weak lower crustal emplacement is consistent with the timescales of crustal flow (Wang *et al.* 2012).

Our Pg-wave Q model, combined with this geological and geophysical evidence and inferences, delineates a consistent and complex evolutionary process in SE Tibet, reflecting the joint effect of the ELIP impeding crustal channel flow and upwelling of hot mantle materials along the Red River Fault and Xiaojiang Fault. During the Permian, magmatic underplating occurred in SE Tibet as a result of mantle plume activity and then gradually cooled, forming intracrustal remnants of mafic magma beneath the CYB (associated with the formation of the ELIP). During the Oligocene, the upper crust thickened along faults due to Cenozoic orogenesis; after that, it took at least 20 Myr of thermal weakening for the thickened crust to attain the viscosity required for crustal material flow (Beaumont *et al.* 2004). Since the Late Miocene, crustal material in the Tibetan Plateau has migrated southeastward through weak channels beneath the Songpan-Ganzi Block and Western Sichuan Block driven by gravity and lateral pressure gradients, and accumulated due to the obstruction of the intracrustal basaltic magma remnants beneath the inner zone of the ELIP, leading to significant crustal thickening and surface uplift. Additionally, the asthenospheric upwelling along the Red River and Xiaojiang Faults interacted with the crust of the western margin of the Yangtze Craton and the Indo-China Plate.

6 CONCLUSION

In this study, we developed a Pg-wave attenuation tomography method using both single- and two-station data and constructed a high-resolution ($0.5^\circ \times 0.5^\circ$) broad-band Q_{Pg} model for the crust in the southeastern margin of the Tibetan Plateau based on 60 025 vertical-component seismograms recorded by a high-density seismic array. The resulting Q_0 values are consistent with those from the two-station method in individual geological blocks, which validated the robustness of our tomographic method. The attenuation structure is correlated with regional structures in geological blocks and provides constraints on the crustal deformation in SE Tibet. Our main findings are as follows:

1. Two mechanically weak zones in the crust are independent of each other and have different origins, suggesting that the crustal channel flow is not connected in this region.
2. The strong attenuation in the Western Sichuan Block and Songpan-Ganzi Block may indicate a mid-lower crustal flow channel, with partial melting or aqueous fluids. The crustal channel flow is blocked by the ELIP and confined to the WSB, which has resulted in the accumulation of ductile material and the development of significant crustal thickening, as well as the topographic uplift in the Western Sichuan Block. The mid-lower crustal flow in SE Tibet does not extend into the foreland Yangtze craton.
3. The strong Pg attenuation across the Red River Fault and Xiaojiang Fault is likely due to asthenospheric upwelling.
4. Since the collision between the Indian plate and the Eurasian plate, the deformation of SE Tibet has experienced a two-stage growing process. During the Oligocene, the upper crust thickened by extrusion along faults. The tectonic mechanism gradually changed from early compression to late extension. From the Late Miocene to the present, crustal material flow through weak channels beneath the Western Sichuan Block driven by gravity and lateral pressure gradients has been the main cause of crustal thickening. Hot mantle materials upwell along the Red River Fault and Xiaojiang Fault, heating and softening the crustal materials, which may become a new mechanism affecting the tectonic evolution of the southeastern Tibetan Plateau.

SUPPORTING INFORMATION

Supplementary data are available at *GJI* online.

Figure S1. (a) Map showing the epicentre of an earthquake that occurred on 25 November 2014, and locations of seismic stations. (b) Normalized vertical-component ground velocity seismograms filtered between 0.01 and 20.0 Hz. The traces are ordered according to their epicentral distances, with station names marked on the left. The red parts of waveforms are sampled by the group velocity window of 6.3–5.4 km s^{-1}. The green dashed line marks the epicentral distance of 800 km.

Figure S2. Inverted site responses at 0.5, 1.0 and 5.0 Hz for all 201 stations used in this study. The magnitudes of these site responses are colour-coded.

Figure S3. Comparison between broad-band (0.5–5.0 Hz) Q_{Pg} maps (a) from combined single- and two-station data (Q_{STS}) and (b) from two-station data only (Q_{TS}). Two revealed low-Q_{Pg} zones, LQZ1 and LQZ2, are circled by white dashed lines in (a). The geological blocks and major faults are labelled. CYB: Central Yunnan Block; EHS: Eastern Himalaya Syntaxis; ICB: Indo-China Block; SB: Sichuan Basin; SGB: Songpan-Ganzi Block; TRB: Three-River Orogenic Belt; WSB: Western Sichuan Block; YJB: Youjiang Basin; YZ: Yangtze Block. JSJF: Jinshajiang Fault; LMSF: Longmenshan Fault; LXF: Lijiang-Xiaojinhe Fault; RRF: Red River Fault; XJF: Xiaojiang Fault; XSHF: Xianshuihe Fault.

Table S1. Earthquake parameters used in this study.

Please note: Oxford University Press is not responsible for the content or functionality of any supporting materials supplied by the authors. Any queries (other than missing material) should be directed to the corresponding author for the paper.

ACKNOWLEDGMENTS

The comments from Editor I. Bastow, Assistant Editor L. Alexander, reviewer C. Singh and an anonymous reviewer are valuable and greatly improved this paper. This research was supported by the National Natural Science Foundation of China (U2139206, 41974061, 41974054) and the Special Fund of China Seismic Experimental Site (2019CSES0103).

DATA AVAILABILITY

The waveforms were collected from the China Earthquake Network Center (CENC), National Earthquake Data Center at http://data.earthquake.cn (last accessed February 2023) for those recorded by the China National Digital Seismic Network (CNDSN) and downloaded from the Incorporated Research Institutions for Seismology Data Management Center (IRIS-DMC) at www.iris.edu (last accessed February 2023) for those recorded by the Global Seismic Network (GSN) and the International Federation of Digital Seismic Networks (FDSN) stations. Certain figures were generated using Generic Mapping Tools (https://forum.generic-mapping-tools.org/, last accessed February 2023; Wessel *et al.* 2013).

CONFLICT OF INTEREST

The authors acknowledge that there are no conflicts of interest recorded.

REFERENCES

Amalokwu, K., Best, A.I., Sothcott, J., Chapman, M., Minshull, T. & Li, X.Y., 2014. Water saturation effects on elastic wave attenuation in porous rocks with aligned fractures, *Geophys. J. Int.,* **197**(2), 943–947.

Bai, D. *et al.*, 2010. Crustal deformation of the eastern Tibetan plateau revealed by magnetotelluric imaging, *Nat. Geosci.,* **3**(5), 358–362.

Bao, X., Song, X., Eaton, D.W., Xu, Y. & Chen, H., 2020. Episodic lithospheric deformation in eastern Tibet inferred from seismic anisotropy, *Geophys. Res. Lett.,* **47**(3), e2019GL085721, doi:10.1029/2019GL085721.

Bao, X.W. *et al.*, 2015. Two crustal low-velocity channels beneath SE Tibet revealed by joint inversion of Rayleigh wave dispersion and receiver functions, *Earth planet. Sci. Lett.,* **415,** 16–24.

Bao, X.Y. *et al.*, 2011a. Pg attenuation tomography within the Northern Middle East, *Bull. seism. Soc. Am.,* **101**(4), 1496–1506.

Bao, X.Y., Sandvol, E., Ni, J., Hearn, T., Chen, Y.S.J. & Shen, Y., 2011b. High resolution regional seismic attenuation tomography in eastern Tibetan Plateau and adjacent regions, *Geophys. Res. Lett.,* **38**(16), doi:10.1029/2011GL048012.

Beaumont, C., Jamieson, R.A., Nguyen, M.H. & Medvedev, S., 2004. Crustal channel flows: 1. Numerical models with applications to the tectonics of the Himalayan-Tibetan Orogen, *J. geophys. Res.,* **109**(B6), doi:10.1029/2003JB002809.

Benz, H.M., Frankel, A. & Boore, D.M., 1997. Regional lg attenuation for the continental United States, *Bull. seism. Soc. Am.,* **87**(3), 606–619.

Bi, X. *et al.*, 2009. Crystallisation conditions (T, P, fO2) from mineral chemistry of Cu- and Au-mineralised alkaline intrusions in the Red River–Jinshajiang alkaline igneous belt, western Yunnan Province, China, *Mineral. Petrol.,* **96**(1), 43–58.

Boore, D.M. & Boatwright, J., 1984. Average body-wave radiation coefficients, *Bull. seism. Soc. Am.,* **74**(5), 1615–1621.

Brune, J.N., 1970. Tectonic stress and the spectra of seismic shear waves from earthquakes, *J. geophys. Res.,* **75**(26), 4997–5009.

Caldwell, W.B., Klemperer, S.L., Rai, S.S. & Lawrence, J.F., 2009. Partial melt in the upper-middle crust of the northwest Himalaya revealed by Rayleigh wave dispersion, *Tectonophysics,* **477**(1-2), 58–65.

Campillo, M., Bouchon, M. & Massinon, B., 1984. Theoretical study of the excitation, spectral characteristics, and geometrical attenuation of regional seismic phases, *Bull. seism. Soc. Am.,* **74**(1), 79–90.

Chen, L. & Gerya, T.V., 2016. The role of lateral lithospheric strength heterogeneities in orogenic plateau growth: insights from 3-D thermo-mechanical modeling, *J. geophys. Res.,* **121**(4), 3118–3138.

Chen, M., Huang, H., Yao, H.J., van der Hilst, R. & Niu, F.L., 2014. Low wave speed zones in the crust beneath SE Tibet revealed by ambient noise adjoint tomography, *Geophys. Res. Lett.,* **41**(2), 334–340.

Chen, Y. *et al.*, 2015. Magmatic underplating and crustal growth in the Emeishan Large Igneous Province, SW China, revealed by a passive seismic experiment, *Earth planet. Sci. Lett.,* **432,** 103–114.

Chung, S.L. & Jahn, B.M., 1995. Plume-lithosphere interaction in generation of the Emeishan flood basalts at the Permian-Triassic boundary, *Geology,* **23**(10), 889–892.

Chung, S.L., Lo, C.H., Lee, T.Y., Zhang, Y.Q., Xie, Y.W., Li, X.H., Wang, K.-L. & Wang, P.-L., 1998. Diachronous uplift of the Tibetan plateau starting 40 Myr ago, *Nature,* **394**(6695), 769–773.

Clark, M.K., House, M.A., Royden, L.H., Whipple, K.X., Burchfiel, B.C., Zhang, X. & Tang, W., 2005. Late Cenozoic uplift of southeastern Tibet, *Geology,* **33**(6), 525–528.

Clark, M.K. & Royden, L.H., 2000. Topographic ooze: building the eastern margin of Tibet by lower crustal flow, *Geology,* **28**(8), 703–706.

Dai, A., Tang, C.C., Liu, L. & Xu, R., 2020. Seismic attenuation tomography in southwestern China: insight into the evolution of crustal flow in the Tibetan Plateau, *Tectonophysics,* **792**. 228589.

Deng, Y.F., Zhang, Z.J., Mooney, W., Badal, J., Fan, W.M. & Zhong, Q., 2014. Mantle origin of the Emeishan large igneous province (South China) from the analysis of residual gravity anomalies, *Lithos,* **204,** 4–13.

Gallegos, A., Ranasinghe, N., Ni, J. & Sandvol, E., 2017. Lg attenuation, frequency dependence and relative site response of the western United

States as revealed by the EarthScope Transportable Array, *Geophys. J. Int.,* **209**(3), 1955–1971.
Gao, L., Wang, Q., Deng, J., Zhang, S. & Yang, Z., 2018. Relationship between orogenic gold mineralization and crustal shearing along Ailaoshan-Red River Belt, southeastern Tibetan plateau: new constraint from paleomagnetism, *Geochem. Geophys. Geosyst.,* **19**(7), 2225–2242.
Gao, Y., Shi, Y.T. & Wang, Q., 2020. Seismic anisotropy in the southeastern margin of the Tibetan Plateau and its deep tectonic significances, *Chinese J. Geophys.,* **63**(3), 802–816.
Han, C.R., Huang, Z.C., Hao, S.J., Wang, L.S., Xu, M.J. & Hammond, J.O.S., 2022. Restricted lithospheric extrusion in the SE Tibetan Plateau: evidence from anisotropic Rayleigh-wave tomography, *Earth planet. Sci. Lett.,* **598,** doi:10.1016/j.epsl.2022.117837.
He, B., Xu, Y.-G., Chung, S.-L., Xiao, L. & Wang, Y., 2003. Sedimentary evidence for a rapid, kilometer-scale crustal doming prior to the eruption of the Emeishan flood basalts, *Earth planet. Sci. Lett.,* **213**(3), 391–405.
He, X., Zhao, L.F., Xie, X.B., Tian, X.B. & Yao, Z.X., 2021. Weak crust in southeast Tibetan plateau revealed by lg-wave attenuation tomography: implications for crustal material escape, *J. geophys. Res.,* **126**(3), doi:10.1029/2020JB020748.
Holt, W.E., Ni, J.F., Wallace, T.C. & Haines, A.J., 1991. The active tectonics of the eastern Himalayan syntaxis and surrounding regions, *J. geophys. Res.,* **96**(B9), 14 595–14 632.
Hou, Z., Zhou, Y., Wang, R., Zheng, Y., He, W., Zhao, M., Evans, N.J. & Weinberg, R.F., 2017. Recycling of metal-fertilized lower continental crust: origin of non-arc Au-rich porphyry deposits at Cratonic edges, *Geology,* **45**(6), 563–566.
Hu, S.B., He, L.J. & Wang, J.Y., 2000. Heat flow in the continental area of China: a new data set, *Earth planet. Sci. Lett.,* **179**(2), 407–419.
Huang, Z.C. *et al.*, 2015. Mantle structure and dynamics beneath SE Tibet revealed by new seismic images, *Earth planet. Sci. Lett.,* **411,** 100–111.
Huang, Z.C., Wang, L.S., Xu, M.J. & Zhao, D.P., 2018. P wave anisotropic tomography of the SE Tibetan plateau: evidence for the crustal and upper-mantle deformations, *J. geophys. Res.,* **123**(10), 8957–8978.
Jiang, G.Z., Hu, S.B., Shi, Y.Z., Zhang, C., Wang, Z.T. & Hu, D., 2019. Terrestrial heat flow of continental China: updated dataset and tectonic implications, *Tectonophysics,* **753,** 36–48.
Karato, S. & Spetzler, H.A., 1990. Defect microdynamics in minerals and solid-state mechanisms of seismic wave attenuation and velocity dispersion in the mantle, *Rev. Geophys.,* **28**(4), 399–421.
Kennett, B.L.N., 1989. On the nature of regional seismic phases-I. Phase representations for pn, pg, Sn, lg, *Geophys. J. Int.,* **98**(3), 447–456.
Kobayashi, M., Takemura, S. & Yoshimoto, K., 2015. Frequency and distance changes in the apparent P-wave radiation pattern: effects of seismic wave scattering in the crust inferred from dense seismic observations and numerical simulations, *Geophys. J. Int.,* **202**(3), 1895–1907.
Kong, L.Y., Gurevich, B., Muller, T.M., Wang, Y.B. & Yang, H.Z., 2013. Effect of fracture fill on seismic attenuation and dispersion in fractured porous rocks, *Geophys. J. Int.,* **195**(3), 1679–1688.
Krishna, V.G. & Ramesh, D.S., 2000. Propagation of crustal-waveguide-trapped pg and seismic velocity structure in the south Indian shield, *Bull. seism. Soc. Am.,* **90**(5), 1281–1294.
Kwiatek, G. *et al.*, 2019. Controlling fluid-induced seismicity during a 6.1-km-deep geothermal stimulation in Finland, *Sci. Adv.,* **5**(5), doi:10.1126/sciadv.aav7224.
Langston, C.A., 1982. Aspects of pn and pg propagation at regional distances, *Bull. seism. Soc. Am.,* **72**(2), 457–471.
Laske, G., Masters, G., Ma, Z. & Pasyanos, M., 2013. Update on CRUST1.0—a 1-degree Global Model of Earth's Crust, in *Paper presented at the EGU General Assembly 2013 Conference,* Abstract, held 7–12 April, 2013 in Vienna, Austria, id. EGU2013-2658.
Lei, J.S., Zhao, D.P., Xu, X.W., Xu, Y.G. & Du, M.F., 2019. Is there a big mantle wedge under eastern Tibet?, *Phys. Earth planet. Inter.,* **292,** 100–113.
Li, W., Chen, Y., Liang, X.F. & Xu, Y.G., 2021. Lateral seismic anisotropy variations record interaction between Tibetan mantle flow and plume-strengthened Yangtze Craton, *J. geophys. Res.,* **126**(4), doi:10.1029/2020JB020841.
Li, X., Ma, X.B., Chen, Y., Xue, S., Varentsov, I.M. & Bai, D.H., 2020. A plume-modified lithospheric barrier to the southeastward flow of partially molten Tibetan crust inferred from magnetotelluric data, *Earth planet. Sci. Lett.,* **548,** doi:10.1016/j.epsl.2020.116493.
Li, Y.J., Liu, M., Li, Y.H. & Chen, L.W., 2019. Active crustal deformation in southeastern Tibetan Plateau: the kinematics and dynamics, *Earth planet. Sci. Lett.,* **523,** doi:10.1016/j.epsl.2019.07.010.
Liu, J., Chen, X., Wu, W., Tang, Y., Tran, M.-D., Nguyen, Q.-L., Zhang, Z. & Zhao, Z., 2015. New tectono-geochronological constraints on timing of shearing along the Ailao Shan-Red River shear zone: implications for genesis of Ailao Shan gold mineralization, *J. Asian Earth Sci.,* **103,** 70–86.
Liu, Q.Y. *et al.*, 2014. Eastward expansion of the Tibetan Plateau by crustal flow and strain partitioning across faults, *Nat. Geosci.,* **7**(5), 361–365.
Liu, Y., Yao, H.J., Zhang, H.J. & Fang, H.J., 2021. The community velocity model V.1.0 of Southwest China, constructed from joint body- and surface-wave travel-time tomography, *Seismol. Res. Lett.,* **92**(5), 2972–2987.
Molnar, P. & Tapponnier, P., 1975. Cenozoic tectonics of Asia: effects of a continental collision, *Science,* **189**(4201), 419–426.
Nicolas, M., Massinon, B., Mechler, P. & Bouchon, M., 1982. Attenuation of regional phases in western Europe, *Bull. seism. Soc. Am.,* **72**(6), 2089–2106.
Ottemöller, L., 2002. Lg wave Q tomography in Central America, *Geophysical Journal International,* **150**(1), 295–302.
Ottemöller, L., Shapiro, N. M., Singh, S. K. & Pacheco, J. F. 2002. Lateral variation of Lg wave propagation in southern Mexico, *Journal of Geophysical Research-Solid Earth,* **107**(B1), doi:10.1029/2001jb000206.
Paige, C. & Sanders, M.A., 1982. LSQR: an algorithm for sparse linear equation and sparse least squares, *ACM Trans. Math. Software,* **8,** 43–71.
Pasyanos, M.E., Matzel, E.M., Walter, W.R. & Rodgers, A.J., 2009b. Broadband lg attenuation modelling in the Middle East, *Geophys. J. Int.,* **177**(3), 1166–1176.
Pasyanos, M.E., Walter, W.R. & Matzel, E.M., 2009a. A simultaneous multiphase approach to determine P-wave and S-wave attenuation of the crust and upper mantle, *Bull. seism. Soc. Am.,* **99**(6), 3314–3325.
Paul, A., Jongmans, D., Campillo, M., Malin, P. & Baumont, D., 1996. Amplitudes of regional seismic phases in relation to crustal structure of the Sierra Nevada, California, *J. geophys. Res.,* **101**(B11), 25 243–25 254.
Pitarka, A., Somerville, P., Fukushima, Y., Uetake, T. & Irikura, K., 2000. Simulation of near-fault strong-ground motion using hybrid Green's functions, *Bull. seism. Soc. Am.,* **90**(3), 566–586.
Pyle, M.L., Walter, W.R. & Pasyanos, M.E., 2017. High-resolution 2D lg and pg attenuation models in the basin and range region with implications for frequency-dependent Q, *Bull. seism. Soc. Am.,* **107**(6), 2846–2858.
Qiao, L., Yao, H.J., Lai, Y.C., Huang, B.S. & Zhang, P., 2018. Crustal structure of Southwest China and Northern Vietnam from ambient noise tomography: implication for the large-scale material transport model in SE Tibet, *Tectonics,* **37**(5), 1492–1506.
Rosenberg, C.L. & Handy, M.R., 2005. Experimental deformation of partially melted granite revisited: implications for the continental crust, *J. Metamorph. Geol.,* **23**(1), 19–28.
Royden, L.H., Burchfiel, B.C., King, R.W., Wang, E., Chen, Z.L., Shen, F. & Liu, Y., 1997. Surface deformation and lower crustal flow in eastern Tibet, *Science,* **276**(5313), 788–790.
Sato, H. & Fehler, M.C., 2012. *Seismic Wave Propagation and Scattering in the Heterogeneous Earth,* Springer Berlin Heidelberg.
Shaw, P. & Orcutt, J., 1984. Propagation of PL and implications for the structure of Tibet, *J. geophys. Res.,* **89**(NB5), 3135–3152.
Shellnutt, J.G., Zhou, M.F., Yan, D.P. & Wang, Y.B., 2008. Longevity of the Permian Emeishan mantle plume (SW China): 1 Ma, 8 Ma or 18 Ma?, *Geol. Mag.,* **145**(3), 373–388.
Singh, C., Jaiswal, N. & Mukhopadhyay, S., 2019. PgQ model for Nepal Himalaya, *Phys. Earth planet. Inter.,* **286,** 13–20.
Singh, C., Singh, A., Mukhopadhyay, S., Shekar, M. & Chadha, R.K., 2011. Lg attenuation characteristics across the Indian Shield, *Bull. seism. Soc. Am.,* **101**(5), 2561–2567.

Steck, L.K., Begnaud, M.L., Phillips, S. & Stead, R., 2011. Tomography of crustal P and S travel times across the western United States, *J. geophys. Res.,* **116**(B11), doi:10.1029/2011JB008260.

Storchak, D.A., Schweitzer, J. & Bormann, P., 2003. The IASPEI standard seismic Phase List, *Seismol. Res. Lett.,* **74**(6), 761–772.

Street, R.L., Herrmann, R.B. & Nuttli, O.W., 1975. Spectral characteristics of the lg wave generated by central United States earthquakes, *Geophys. J. R. astr. Soc.,* **41**(1), 51–63.

Sun, X.X. *et al.*, 2014. Crustal structure beneath SE Tibet from joint analysis of receiver functions and Rayleigh wave dispersion, *Geophys. Res. Lett.,* **41**(5), 1479–1484.

Sun, Y., Niu, F.L., Liu, H.F., Chen, Y.L. & Liu, J.X., 2012. Crustal structure and deformation of the SE Tibetan plateau revealed by receiver function data, *Earth planet. Sci. Lett.,* **349,** 186–197.

Tapponnier, P. *et al.*, 1990. The Ailao Shan/Red River metamorphic belt: tertiary left-lateral shear between Indochina and South China, *Nature,* **343**(6257), 431–437.

Tapponnier, P., Xu, Z.Q., Roger, F., Meyer, B., Arnaud, N., Wittlinger, G. & Jingsui, Y., 2001. Oblique stepwise rise and growth of the Tibet plateau, *Science,* **294**(5547), 1671–1677.

Walter, W.R., Mayeda, K., Malagnini, L. & Scognamiglio, L., 2007. Regional body-wave attenuation using a coda source normalization method: application to MEDNET records of earthquakes in Italy, *Geophys. Res. Lett.,* **34**(10), doi:10.1029/2007GL029990.

Wang, E., Burchfiel, B.C., Royden, L.H., Chen, L., Chen, J., Li, W. & Zhiliang, C., 1998. *Late Cenozoic Xianshuihe-Xiaojiang, Red River, and Dali Fault Systems of Southwestern Sichuan and Central Yunnan, China*Vol. **327,** Geological Society of America.

Wang, E., Kirby, E., Furlong, K.P., van Soest, M., Xu, G., Shi, X., Kamp, P.J.J. & Hodges, K.V., 2012. Two-phase growth of high topography in eastern Tibet during the Cenozoic, *Nat. Geosci.,* **5**(9), 640–645.

Wang, T.J., Xie, X. & Ji, L.F., 2021. Stochastic finite-fault simulation of the Ms 7.0 Lushan earthquake based on frequency- and distance-dependent radiation patterns, *Bull. seism. Soc. Am.,* **111**(6), 3387–3402.

Wessel, P., Smith, W., Scharroo, R., Luis, J. & Wobbe, F., 2013. Generic mapping tools: improved version released, *EOS, Trans. Am. geophys. Un.,* **94**(45), 409–410.

Winkler, K.W. & Nur, A., 1982. Seismic attenuation: effects of pore fluids and frictional sliding, *Geophysics,* **47**(1), 1–15.

Wu, Y.Q. *et al.*, 2022. High-precision vertical movement and three-dimensional deformation pattern of the Tibetan plateau, *J. geophys. Res.,* **127**(4), doi:10.1029/2021JB023202.

Xie, J., Gok, R., Ni, J. & Aoki, Y., 2004. Lateral variations of crustal seismic attenuation along the INDEPTH profiles in Tibet from lg Q inversion, *J. geophys. Res.,* **109**(B10), doi:10.1029/2004JB002988.

Xie, J. & Mitchell, B.J., 1990. Attenuation of multiphase surface waves in the basin and range province: part I. Lg and lg coda, *Geophys. J. Int.,* **102**(1), 121–137.

Xu, M.J., Huang, Z.C., Wang, L.S., Xu, M.J., Zhang, Y.Q., Mi, N., Yu, V. & Yuan, X., 2020. Sharp lateral moho variations across the SE Tibetan margin and their implications for plateau growth, *J. geophys. Res.,* **125**(5), doi:10.1029/2020JB020745.

Xu, Y.G., He, B., Chung, S.L., Menzies, M.A. & Frey, F.A., 2004. Geologic, geochemical, and geophysical consequences of plume involvement in the Emeishan flood-basalt province, *Geology,* **32**(10), 917–920.

Yang, G., Zhao, L.F., Xie, X.B., Zhang, L. & Yao, Z.X., 2021a. High-precision relocation with the burial depths of the North Korean underground nuclear explosions by combining pn and pg differential travel-times, *J. geophys. Res.,* **126**(6), doi:10.1029/2020JB020745.

Yang, X.Y., Li, Y.H., Afonso, J.C., Yang, Y.J. & Zhang, A.Q., 2021b. Thermochemical State of the upper mantle beneath South China from multi-observable probabilistic inversion, *J. geophys. Res.,* **126**(5), doi:10.1029/2020JB021114.

Yao, H.J., Beghein, C. & van der Hilst, R.D., 2008. Surface wave array tomography in SE Tibet from ambient seismic noise and two-station analysis - II. Crustal and upper-mantle structure, *Geophys. J. Int.,* **173**(1), 205–219.

Yu, N., Unsworth, M., Wang, X.B., Li, D.W., Wang, E.C., Li, R.H., Hu, Y. & Cai, X., 2020. New insights into crustal and mantle flow beneath the Red River fault zone and adjacent areas on the southern margin of the Tibetan plateau revealed by a 3-D magnetotelluric study, *J. geophys. Res.,* **125**(10), doi:10.1029/2020JB019396.

Zhang, L.-S. & Schärer, U., 1999. Age and origin of magmatism along the cenozoic Red River shear belt, China, *Contrib. Mineral. Petrol.,* **134**(1), 67–85.

Zhang, P.Z., Shen, Z., Wang, M., Gan, W.J., Burgmann, R. & Molnar, P., 2004. Continuous deformation of the Tibetan Plateau from global positioning system data, *Geology,* **32**(9), 809–812.

Zhang, Y.Q. & Xie, Y.W., 1997. Nd, Sr isotopic character and chronology of Red River-Jinshajiang alkali-rich intrusive rocks, *Sci. China,* **27**(4), 289–293 (in Chinese).

Zhang, Z.C., Zhi, X.C., Chen, L., Saunders, A.D. & Reichow, M.K., 2008. Re-Os isotopic compositions of picrites from the Emeishan flood basalt province, China, *Earth planet. Sci. Lett.,* **276**(1-2), 30–39.

Zhang, Z.Q., Yao, H.J. & Yang, Y., 2020. Shear wave velocity structure of the crust and upper mantle in Southeastern Tibet and its geodynamic implications, *Sci. China-Earth Sci.,* **63**(9), 1278–1293.

Zhao, L.F. & Mousavi, S.M., 2018. Lateral variation of crustal lg attenuation in Eastern North America, *Sci. Rep.,* **8,** doi:10.1038/s41598-018-2564 9-5.

Zhao, L.F. & Xie, X.B., 2016. Strong lg-wave attenuation in the Middle East continental collision orogenic belt, *Tectonophysics,* **674,** 135–146.

Zhao, L.F., Xie, X.B., He, J.K., Tian, X.B. & Yao, Z.X., 2013. Crustal flow pattern beneath the Tibetan Plateau constrained by regional lg-wave Q tomography, *Earth planet. Sci. Lett.,* **383,** 113–122.

Zhao, L.F., Xie, X.B., Wang, W.M., Zhang, J.H. & Yao, Z.X., 2010. Seismic lg-wave Q tomography in and around Northeast China, *J. geophys. Res.,* **115**(B8), doi:10.1029/2009JB007157.

Zhao, Y., Guo, L.H., Guo, Z., Chen, Y.J., Shi, L. & Li, Y.H., 2020. High resolution crustal model of SE Tibet from joint inversion of seismic P-wave travel-times and Bouguer gravity anomalies and its implication for the crustal channel flow, *Tectonophysics,* **792,** doi:10.1016/j.tecto.2020.228580.